Investigations on the second-order transient gap resonance induced by focused wave groups

Jinshi Liu [a], Junliang Gao [a, b*], Huabin Shi [b], Jun Zang [c], Qian Liu [a]

[a] School of Naval Architecture and Ocean Engineering, Jiangsu University of Science and Technology, Zhenjiang 212003, China

[b] State Key Laboratory of Internet of Things for Smart City and Department of Civil and Environmental Engineering, University of Macau, Macao 999078, China

[c] Centre for Infrastructure, Geotechnical and Water Engineering (IGWE), Department of Architecture and Civil Engineering, University of Bath, BA2 7AY, UK

Abstract:

Two or more marine structures deployed side by side may encounter strong water-body resonances within narrow gaps between them. It may cause significant wave loads on structures and the green water phenomenon on the deck. In this article, the transient fluid motion within a narrow gap formed by two fixed boxes suffered from incident focused wave groups is investigated using a two-dimensional viscous flow numerical wave flume. The focused wave groups adopted have the spectral peak frequency equal to half the fluid resonant frequency inside the gap. The wave fields both inside the gap and around the two-box system, the response/damping time of the transient wave surfaces inside the gap, the maximum wave forces and the ratios of the 2^{nd}-order to the corresponding 1^{st}-order wave surfaces/forces are investigated. It is revealed that the most dangerous place to green water is always the front edge of the two-box system. The damping time of the 2^{nd}-order wave surface is significantly larger than that of the 1^{st}-order one. As the incident wave amplitude rises, the ratios of the 2^{nd}-order to the first-order wave surfaces/forces becomes increases gradually and can even exceed 100% for the wave surface, the horizontal wave force and the moment.

Keywords: Transient gap resonance; Second-order resonance; Focused wave groups; Wave amplification; Wave loads; OpenFOAM®

* Corresponding author. Email: gaojunliang880917@163.com (J. Gao)

1. Introduction

For two or more marine structures deployed side by side and suffered from ocean surface waves, if there exist narrow gaps between them, large-amplitude piston-mode free surface oscillations can occur within the gaps at certain frequencies, which is normally called "*gap resonance*". The phenomenon may cause extremely large wave elevations in the gaps and wave loads on the structures (Ning et al., 2018; Zhu et al., 2005). Therefore, much attention should be paid to the operational and/or structural safety for the multiple structures arranged side by side and very closely to each other, and correspondingly, more investigations need to be implemented to expand the understanding of gap resonance.

At the early stage, theoretical analyses were widely adopted to study this phenomenon, and almost all the theoretical investigations were based on the linear potential flow theory (e.g. Miao et al. (2000); Molin (2001); Zhu et al. (2006)). To examine the previous theoretical researches and obtain a better comprehension on the phenomenon, numerous laboratory experiments were also carried out. Saitoh et al. (2006) and Iwata et al. (2007) implemented a series of two-dimensional (2D) experiments in physical wave flumes to analyze the fluid resonance occurring in a narrow gap formed by two boxes and that in two narrow gaps formed by three boxes, respectively. A series of 2D physical experiments were also conducted by Tan et al. (2014), Zhang et al. (2021a) and Milne et al. (2022) to investigate the gap resonance between a box-shaped ship cross-section and a vertical quay. In addition, a few three-dimensional (3D) experiments were also carried out by Li et al. (2016), Zhao et al. (2017) and Huang et al. (2020) to study the fluid resonance between two barges or inside a moonpool.

Heretofore, most numerical studies on gap resonance adopted the classical potential flow theory (CPFT) combining with different numerical discretization techniques (e.g., Li and Zhang (2016); Sun et al. (2010)). Nevertheless, due to the neglect of the flow viscosity in the CPFT, the simulations based on them remarkably over-predict the wave elevation within the narrow gap and hence the wave forces acting on the structure (Kristiansen and Faltinsen, 2008). To address this disadvantage, some special techniques were proposed so that the energy dissipation can be added into the CPFT artificially (e.g., Ning et al. (2015); Tan et al. (2019); Wang et al. (2022)). With the fast development of computer technology, the numerical investigations based on the CFD (Computational Fluid Dynamics) simulations are becoming more and more prevalent in recent years. Based on a domain-decomposition method, Kristiansen and Faltinsen (2012) developed a solver that can couple the Navier–Stokes equations with the potential theory, and the solver provides an effective tool to analyze gap resonance problems in the real engineering scale. Based on some in-house or open-sourced or commercial CFD models, different aspects of the gap resonance phenomenon have been widely studied by many scholars (e.g., Gao et al. (2019a); Gao et al. (2019b); He et al. (2021b); Jiang et al. (2018); Lu et al. (2011a); Lu et al. (2011b); Zhang et al. (2021b)), and it has been found that the CFD-based simulation results coincide with available experimental ones very well.

Although many investigations on the phenomenon have been performed, most of them were concerned only on the steady-state gap resonance triggered by the incident steady-state regular or irregular waves (e.g., Chua et al. (2018); Ding et al. (2022); Gao et al. (2020b); He et al. (2021a); He et al. (2022); Jiang et al. (2021); Song et al. (2021); Zhao et al. (2021)). In contrast, only a few scholars performed the transient gap resonance investigations excited by transient wave groups. Based on a potential flow solver, the transient gap resonance was preliminarily studied in Taylor et al. (2008), and only simple comparisons between the incident focused waves and the free-surface elevations within the gap were made therein. Recently, various aspects of the resonant wave surface within the gap formed in between two fixed barges triggered by focused waves were experimentally investigated by Zhao et al. (2017; 2020). The resonant amplitudes and frequencies, mode shapes, the group dynamics and higher harmonics of fluid motions inside the gap were deeply studied in both papers. The mechanisms of the nonlinear interactions between different harmonic components and the various driven mechanisms of gap resonance were well revealed. The experiments of Zhao et al. (2017) were successfully reproduced by Wang et al. (2018) based on the open-sourced OpenFOAM® model. More recently, also based on OpenFOAM®, the so called 1st-order transient gap resonance phenomenon between two fixed boxes excited by focused waves was simulated in Gao et al. (2020a), where the incident focused waves always had the spectral peak frequency equal to the fluid resonant frequency of the gap. The amplification and the response/damping time of the wave surface, the maximum wave loads and the relative importance of the high-order wave loads to the first-order ones were investigated therein.

To boost the knowledge and understanding of the hydrodynamic phenomena related to transient gap resonance, this paper further investigates the transient gap resonance excited by focused wave groups. Similar to Gao et al. (2020a), the amplification and the response/damping time of the wave surface, the maximum wave elevations/loads and the relative importance of the high-order to the first-order wave elevations/loads are also investigated here. However, different from the previous work, the spectral peak frequency of the incident focused wave groups adopted in this article is no longer equal to the fluid resonant frequency of the gap, but instead the former is set to half of the latter. Due to the quadratic coupling of the linear wave components, the spectral peak frequency of the 2^{nd}-order sum harmonic wave components coincides with the fluid resonant frequency of the gap, and the so-called 2^{nd}-order gap resonance phenomenon could be triggered (Ding et al., 2022; He et al., 2021a; Zhao et al., 2017). Although the 2^{nd}-order transient gap resonance excited by focused wave groups has been investigated in Zhao et al. (2017) and Wang et al. (2018), only the wave elevations within the gap were recorded and analyzed therein. As far as the authors know, aiming at the 2^{nd}-order transient gap resonance phenomenon, the wave elevations in the vicinity of (i.e., in the front or at the rear of) the multi-structure system and the wave forces impacting on the structure have heretofore not been investigated. Both similarities and differences between the hydrodynamic features in the present study and those in Gao et al. (2020a) will also be compared and analyzed in this article.

Similar to Gao et al. (2020a), all simulations in this paper are performed by adopting the OpenFOAM® model and a 2D numerical wave flume (NWF). Both the NewWave theory of Tromans et al. (1991) and the phase/amplitude correction technique of Fernández et al. (2014) are utilized to generate the desired incident focused wave groups. The four-phase combination analysis technique of Fitzgerald et al. (2014) is used to decompose both wave elevations and wave loads into the lowest four order harmonic components during the 2^{nd}-order transient gap resonance.

The rest of this article is organized as follows. Section 2 briefly introduces the numerical model and the four-phase combination analysis technique. Section 3 describes the setups of both the NWF and the incident wave parameters in detail. Section 4 presents the simulation results and discussions. Finally, main conclusions are drawn in Section 5.

2. Numerical model and analysis technique

2.1 Numerical model

All simulations in this paper are carried out by utilizing OpenFOAM® version 3.0.1. Both the "*interFoam*" multiphase flow solver built in the model and a third-party wave-making toolboox "*waves2Foam*" of Jacobsen et al. (2012) are adopted to track the free water surface and produce/dissipate waves.

Fig. 1 illustrates the NWF, its boundary conditions and the layout of relaxation zones utilized in present study. The inlet boundary prescribes both the elevation of air/water interface and the velocities of water particles based on desired wave theories, and the zero pressure gradient is also set therein. The "no-slip" boundary condition is defined at all the solid-wall-type boundaries which include the right and bottom boundaries of the NWF and all edges of both boxes. Near the inlet/outlet boundaries, the so-called "relaxation zones" are deployed to absorb the energy of outgoing waves. The upper part of the NWF prescribes the "atmosphere" boundary condition. To establish a 2D flume, the "empty" boundary condition is defined at both the front and back boundaries. As in Moradi et al. (2015) and Gao et al. (2021), the largest Courant number allowed in the model is set to 0.25 for all simulations.

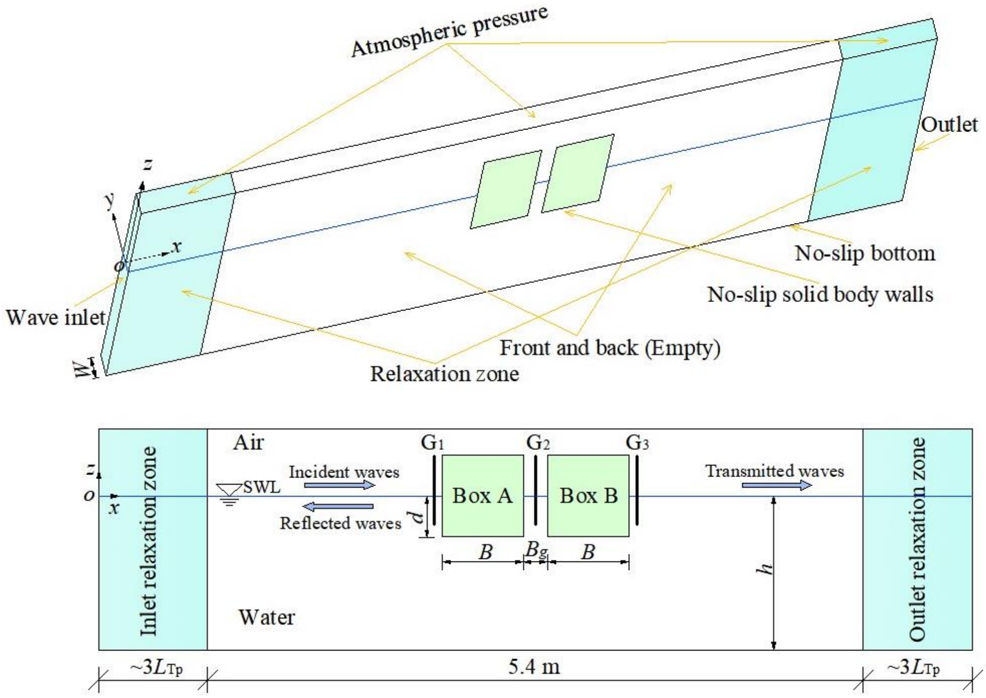

Fig. 1. The NWF adopted in the present study: (a) the boundary conditions and the coordinate system; (b) the layouts of wave gauges and relaxation zones.

It is noted here that the wave loads considered in this article include horizontal wave forces, vertical wave forces and wave moments impacting on the two boxes, and that the moments on both boxes correspond to their respective centroid.

2.2 Analysis technique

The current work adopts the four-phase combination analysis technique of Fitzgerald et al. (2014) to decompose the total wave elevations and wave loads into the lowest four order harmonic components during the 2nd-order transient gap resonance. To make readers better understand this article, this analysis technique is briefly introduced here.

In the analysis technique, a narrow-banded wave power spectrum is assumed. Both the wave-wave interaction and the wave-structure interaction can then be described by a Stokes-type expansion, formulated up to the 4th order here:

$$F(\theta) = Af_{11}\cos\theta + A^2(f_{20} + f_{22}\cos 2\theta) + A^3(f_{31} + f_{33}\cos 3\theta) + A^4(f_{42} + f_{44}\cos 3\theta) + O(A^5)\,, \quad (1)$$

where F denotes the time series of wave surfaces or wave loads, A denotes the linear component amplitude, f_{ij} denotes some coefficients appearing in the expansion, and θ denotes the phase function of the incident focused waves.

Four incident focused wave groups are produced by the same wave-making signal except that the phase of each Fourier component is shifted by 0, $\pi/2$, π and $3\pi/2$, and the corresponding four time series of wave elevations or wave loads, F_0, $F_{\pi/2}$, F_π and $F_{3\pi/2}$ are generated and recorded. The lowest four order harmonic components of the signal of interest can then be obtained via a linear combination of its corresponding four signals excited by the four-phase focused wave groups mentioned above, and can be expressed as follows:

$$1^{\text{st}}\text{ sum harmonic: } (Af_{11} + A^3 f_{31})\cos\theta + O(A^5) = \frac{(F_0 - F^{\mathrm{H}}_{\pi/2} - F_\pi + F^{\mathrm{H}}_{3\pi/2})}{4}, \quad (2)$$

$$2^{\text{nd}}\text{ sum harmonic: } (A^2 f_{22} + A^4 f_{42})\cos 2\theta + O(A^6) = \frac{(F_0 - F_{\pi/2} + F_\pi - F_{3\pi/2})}{4}, \quad (3)$$

$$3^{\text{rd}}\text{ sum harmonic: } A^3 f_{33}\cos 3\theta + O(A^5) = \frac{(F_0 + F^{\mathrm{H}}_{\pi/2} - F_\pi - F^{\mathrm{H}}_{3\pi/2})}{4}, \quad (4)$$

$$2^{\text{nd}}\text{ diff. } +4^{\text{th}}\text{ sum harmonics: } A^2 f_{20} + A^4 f_{44}\cos 4\theta + O(A^6) = \frac{(F_0 + F_{\pi/2} + F_\pi + F_{3\pi/2})}{4}, \quad (5)$$

in which the superscript "H" denotes the Hilbert transform of the signal. For more detailed information on the theory of the analysis technique, the interested reader is referred to Fitzgerald et al. (2014).

Since the analysis technique was put forward by Fitzgerald et al. (2014), it has been successfully utilized to extract the harmonic components of both wave elevations and wave loads around/on various types of marine structures suffered from focused wave groups (e.g., Chen et al. (2019); Chen et al. (2021); Feng et al. (2020); Zhao et al. (2017)).

3. Numerical wave flume

As mentioned in Section 2, a 2D NWF is established in this article for all simulations (see Fig. 1). A Cartesian coordinate system with the origin, o, at the SWL (still water level) of the inlet boundary is defined. The $+x$ axial direction coincides with the propagation direction of the incident waves, the $+y$ axial direction parallels with the width of the flume and points toward the back boundary, and the $+z$ axis points vertically upwards. The length and the height of the flume are 35.0 m and 0.8 m, respectively. To simulate the 2D problem, only one computational cell is deployed along the y axis, and the width of the flume is set to W=0.01 m. At the middle of the NWF, a two-box system consisting of two identical fixed boxes is installed. Their draft d, height H and breadth B are respectively 0.25 m, 0.50 m and 0.50 m. The width of the narrow gap formed in between the two boxes is B_g=0.05 m. The still water depth is set to h=0.50 m.

The above-mentioned layouts for both the two-box system and the still water depth are identical to the corresponding experimental/numerical setups in Saitoh et al. (2006) and Lu et al. (2011b) where the steady-state gap resonance triggered by monochromatic waves was studied. According to the two literatures, the fluid resonant frequency of the narrow gap presented in Fig. 1 is ω_R =5.285 rad/s. In this article, to successfully trigger the 2nd-order transient gap resonance, the spectral peak frequency of the incident focused wave group is set to ω_p=0.5ω_R=2.643 rad/s (it will be described in detail in the next paragraph), so that the double frequency of ω_p coincides with the fluid resonant frequency of the gap. Based on the linear dispersion relationship, the wavelength of the wave component with the spectral peak frequency is L_p=4.95 m. Two relaxation zones with an identical length are placed around the inlet/outlet boundaries, and the length of each relaxation zone is set to 14.80 m (about 3L_p) to ensure the satisfactory dissipation for the outgoing waves. Three wave gauges (G_1 – G_3) are installed in the flume. G_2 is placed in the middle of the narrow gap to record the fluid resonance. G_1 and G_3 are deployed very closely to the upstream of Box A and the downstream of Box B, respectively, with the distance of only 0.005 m from the edge of each box.

In present study, the NewWave theory of Tromans et al. (1991) is adopted to generate focused wave groups. The wave groups include numerous cosine wave components with various frequencies, and these components focus at a specific point both in space and in time. If the wave nonlinearity is ignored, the elevation of a focused wave group can be formulated as follows:

$$\eta(x,t)=\sum_{n=1}^{N}a_n\cos\varphi_n\ , \tag{6}$$

in which

$$a_n=A_{\mathrm{f}}\frac{S(\omega_n)\times\Delta\omega}{\sum_{n=1}^{N}S(\omega_n)\times\Delta\omega}, \tag{7}$$

$$\varphi_n=k_n(x-x_{\mathrm{f}})-\omega_n(t-t_{\mathrm{f}})+\varphi_0\,. \tag{8}$$

In these equations, N=100 refers to the number of the cosine wave components considered. A_{f} is the focused wave amplitude and ranges from 0.01 m to 0.10 m with an increment of 0.01 m. a_n, k_n and ω_n respectively refer to the wave amplitude, the wavenumber and the circular frequency for the n^{th} cosine component. $\Delta\omega$ is the frequency difference between adjacent cosine components. t_{f} =15.0 s and x_{f} =17.50 m (i.e., at gauge G_2) are the focusing time and the focusing place, respectively. φ_0 denotes the phase angle and is set to zero for a crest-focused wave group. $S(\omega_n)$ denotes the wave power spectrum.

The JONSWAP spectrum of Hasselmann et al. (1973) formulated as

$$S(\omega_n)=\alpha g^2\frac{1}{\omega_n^5}\exp\left[-\frac{5}{4}\left(\frac{\omega_{\mathrm{p}}}{\omega_n}\right)^4\right]\times\gamma^{\beta} \tag{9}$$

is adopted in this article, in which α=0.0081 and

$$\beta=\exp\left[-(\omega_n-\omega_{\mathrm{p}})^2\Big/\left(2\sigma^2\omega_{\mathrm{p}}^2\right)\right]. \tag{10}$$

ω_{p} denote the spectral peak circular frequency, which is set to 2.643 rad/s for all simulations so that the 2nd-order transient fluid resonance in the gap can be excited. σ is set to 0.07 when $\omega_n \le \omega_{\mathrm{p}}$ and otherwise to 0.09. γ denotes the peak enhancement factor that is set to 3.3 in this paper.

It should be stressed here that, due to that Eq. (6) ignores the effect of the wave nonlinearity, all the actual focusing time, focusing place, focused wave amplitude would have a certain degree of deviations from the desired ones. To ensure that the incident focused wave groups generated in the wave inlet boundary accurately possess the desired focusing time, focusing place and focused amplitude, the methodology of Fernández et al. (2014) to iteratively correct both wave amplitude and the phase is also adopted. Due to limited space, its specific principle is not presented here.

Meshes in the NWF are produced by "*blockMesh*" which is a mesh-generating utility built in the numerical model. Typical mesh layout in the vicinity of the boxes is shown in Fig. 2. To model the propagation of the incident waves and track the free water surface accurately, the cell size becomes smaller and smaller from the bottom/atmosphere boundaries to the SWL. Compared to the meshes at the two pure wave propagation regions in the front of and at the rear of the two-box system, finer meshes are deployed around the two boxes, especially within the gap.

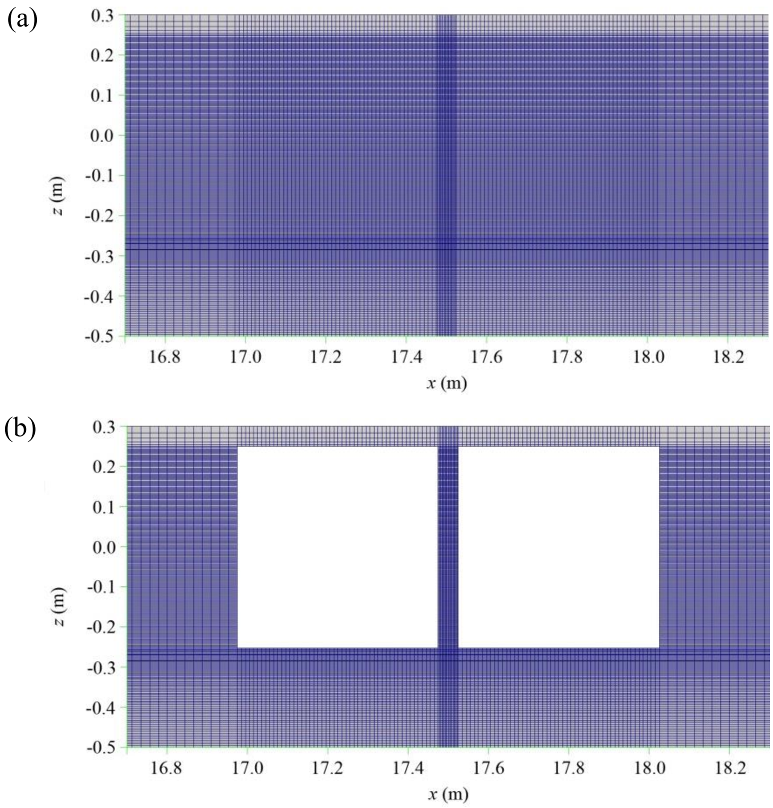

Fig. 2. Typical mesh layout at the middle area of the NWF: (a) without the box; (b) with the two-box system

The convergence analysis for the simulation results is performed by utilizing four sets of meshes (i.e., Meshes 1–4) with gradually finer resolutions. Aiming at the NWF without the box, the cell numbers for Meshes 1–4 are 193420, 331580, 426540 and 558670, respectively. The cell numbers of the NWF with boxes for the four meshes are slightly less than the corresponding ones of the NWF without the box because of the detachment of the cells within the two boxes from the computational domain. Figs. 3 and 4 present the time series of wave elevations at gauge G_2 under Meshes 1–4 for the NWFs without and with the two-box system, respectively. The simulated incident wave group in both figures is crest-focused (i.e., φ_0=0) and has A_f=0.03 m. For Meshes 1–3, slightly differences between their wave elevations are observed at both the focusing crest and the following trough. As the mesh becomes denser, the wave elevations for Meshes 3 and 4 become almost exactly coincident with each other. It shows that Mesh 3 obtains convergent results, and hence is chosen for all simulations.

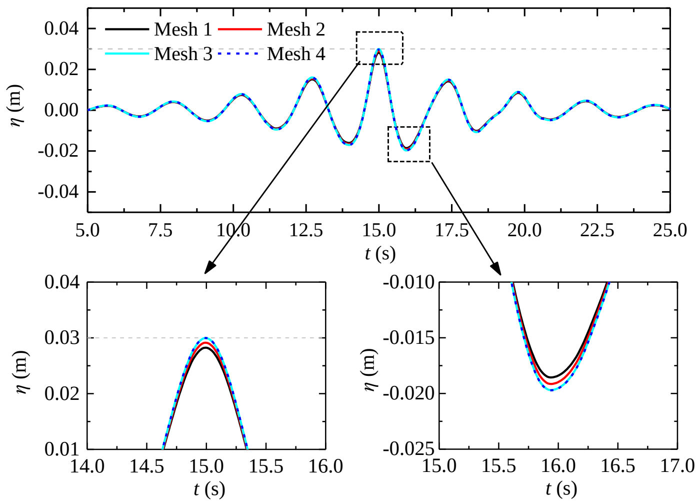

Fig. 3. Time series of the wave elevations at gauge G_2 under Meshes 1–4 for the NWF without the box suffered from the incident crest-focused wave groups with A_f=0.03 m

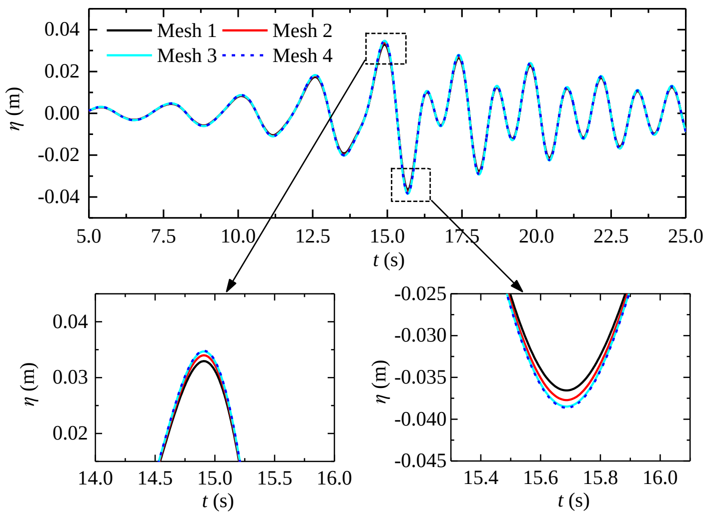

Fig. 4. As in Fig. 3, but for the NWF with the two-box system

Prior to performing the present investigations on the 2nd-order gap resonance phenomenon, the accuracy of the numerical model in simulating the nonlinear wave-structure interaction is examined. Rodríguez et al. (2016) carried out a series of experiments in a physical wave flume with a length of 63 m and a width of 2.79 m. The water depth in the wave flume was h=1.25 m. A box was fixed at around the middle of the wave flume. The box has a breadth of B=0.50 m and a draught of d=0.25 m. The width of the box along the width direction of the wave flume was 2.76 m, which leaves only 0.015 m to each sidewall of the wave flume. Two sets of the incident regular waves with kA_0 = 0.05 and 0.10 were considered, where k and A_0 are the wavenumber and the wave amplitude of the incident regular waves, respectively.

To test the capability of OpenFOAM® to reproduce strong wave-structure interactions, the interactions between the box and the incident waves with kA_0 = 0.10 are simulated here. Due to the identical breadth and draught of the box used in the physical experiments to those of the two boxes studied in this paper, a NWF very similar to that in Fig. 1 (not shown here for brevity) is utilized to perform the simulations. Different from the NWF shown in Fig. 1, only one box is placed in the middle of the flume. In addition, as in the physical wave flume, the water depth in the NWF is set to 1.25 m. A mesh with a similar density to Mesh 3 is adopted. The comparisons between the experimental data of Rodríguez et al. (2016) and the simulation results of the present numerical model for both the 1st-order and the 2nd-order vertical wave forces acting on the box are presented in Fig. 5, and a good agreement between them is seen.

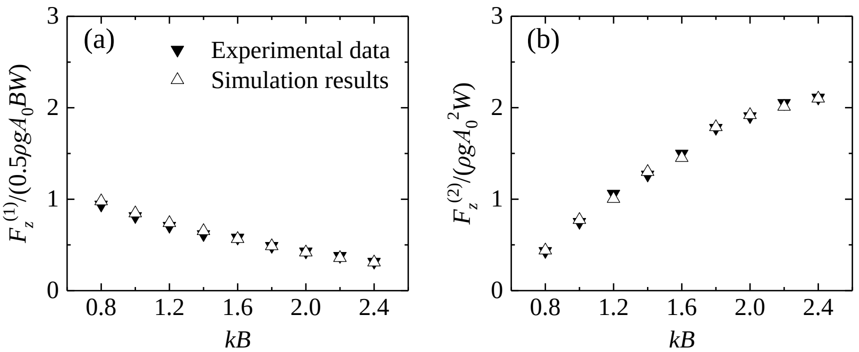

Fig. 5. The comparisons between the experimental data of Rodríguez et al. (2016) and the simulation results of OpenFOAM® for (a) the normalized 1st-order and (b) the normalized 2nd-order vertical wave forces induced by the incident regular waves with kA_0=0.10.

4. Numerical results and discussion

To gain an overall understanding on the features of wave fields, not only the fluid magnification within the gap but also the variations of the wave elevations around the two-box system due to the existence of the two boxes are first shown in subsection 4.1, where the response/damping time of the first two order sum harmonic components of the wave elevation within the gap are also quantitatively estimated. Subsequently, the three types of wave loads on both boxes (including the horizontal wave forces, the vertical wave forces, and the wave moments) are investigated in subsections 4.2–4.4, respectively. In all the four subsections (i.e., 4.1–4.4), the results in each subsection are presented in the following way, overall. That is, the time series of total physical quantities (wave elevations or wave loads) and their maximum values in the positive and/or the negative directions are first analyzed, and subsequently, the first four order harmonic components are extracted and the first two order sum harmonics are carefully analyzed. Finally, the importance of high-order harmonics (represented by the 2nd-order sum harmonics) relative to first-order ones for all the four physical quantities (i.e., wave elevations, the horizontal wave forces, the vertical wave forces, and the wave moments) is compared in subsection 4.5.

4.1. Wave elevations around the two-box system

4.1.1. Total wave elevations

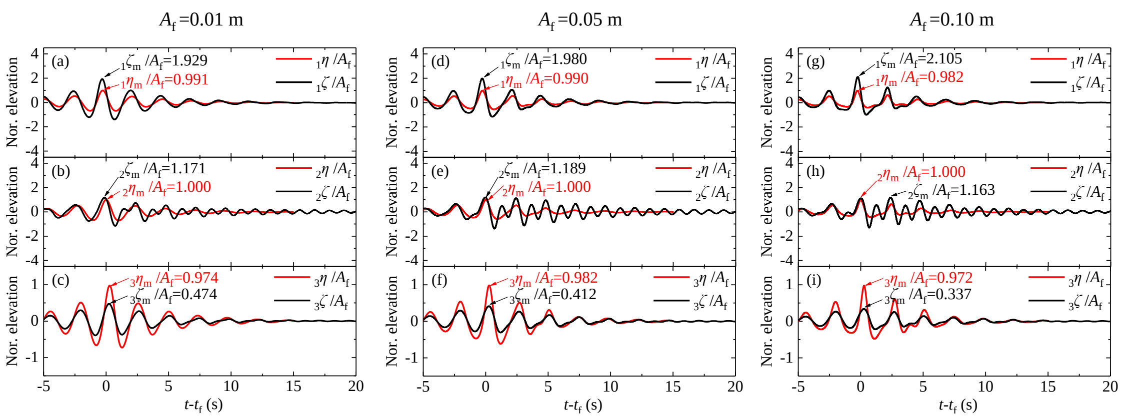

Fig. 6. Comparisons of the time series of total wave elevations under the two conditions of with/without the two-box system at all the three gauges for the crest-focused wave groups with (a–c) A_f=0.01 m, (d–f) A_f=0.05 m, and (g–i) A_f=0.10 m. ${}_i\eta_m$ and ${}_i\zeta_m$ denote the maximum total wave elevations at the gauge G_i (i=1, 2 and 3) without and with the two-box system, respectively.

Fig. 6 compares the time series of the total wave elevations under the two conditions of with/without the two-box system at gauges G_1–G_3 subjected to the incident crest-focused wave groups with A_f=0.01 m, 0.05 m and 0.10 m, which directly show how the existence of the two-box system influence the wave fields not only in the narrow gap but also around the system. The following phenomena can be observed. First, at G_1 (Fig. 6a, d and g), owing to the reflection occurring at the front edge of Box A, the normalized maximum wave elevations for the two-box system (${}_1\zeta_m/A_f$) are remarkably higher than the corresponding ones for the no-box system (${}_1\eta_m/A_f$). The former is around 2.0 for all the three cases, while the latter is always slightly less than 1.0. Second, at G_2 (Fig. 6b, e and h), the normalized maximum wave elevations for the two-box system (${}_2\zeta_m/A_f$) is always less than 1.2, much lower than that at G_1. Compared to the incident focused wave groups (${}_2\eta$), the fluid motion in the gap (${}_2\zeta$) lasts for a much longer time after reaching the maximum elevation, which is similar to the related finding in Taylor et al. (2008) and Gao et al. (2020a) where the 1st-order transient gap resonance triggered by focused waves is concerned. Third, at G_3 (Fig. 6c, f and i), the maximum wave elevation with the two-box system (${}_3\zeta_m$) is shown to be notably lower than the corresponding one of the incident wave group (${}_3\eta_m$), which can be attributed to the occlusion effect of the two-box system for the incident wave group.

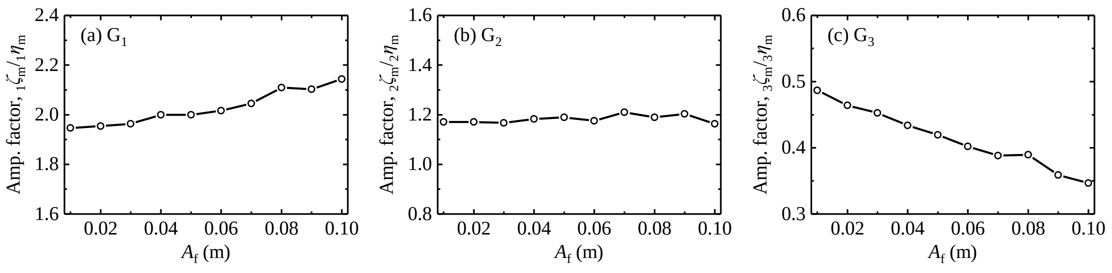

Fig. 7. Variations of the amplification factor of the wave elevations with respect to A_f at (a) G_1, (b) G_2, and (c) G_3

Fig. 7 presents the variations of the amplification factor of the wave elevation defined as ${}_i\zeta_m/{}_i\eta_m$ (i=1, 2 and 3) with respect to A_f at the three wave gauges. For G_1 (Fig. 7a), the amplification factor gradually increases from 1.95 to 2.15 with the rise of the focused wave amplitude, A_f. For G_2 (Fig. 7b), however, the amplification factor there seems insensitive to A_f, and basically maintains a slight fluctuation around 1.90. Different from both G_1 and G_2, the amplification factor for G_3 shows a gradual decline from 0.49 to 0.35 (Fig. 7c). It is clear that the fluid oscillation behind the two-box system has the least possibility to cause the green water on the deck due to the smallest amplification factor of wave elevation therein. On the contrary, the wave elevation at G_1 always shows the largest amplification factor, which implies that the greatest possibility for the green water probably always appears in front of the two-box system.

To confirm the above speculation, Fig. 8 directly compares the normalized maximum wave elevations at G_1 and G_2 inside the NWF with the two-box system for all the incident focused wave amplitudes considered. It can be intuitively observed that the maximum wave elevation at G_1 is indeed always significantly higher than the corresponding one at G_2, no matter whether the incident focused wave amplitude is small or large. The ratio of the former to the latter (i.e., ${}_1\zeta_m/{}_2\zeta_m$) is also shown here. It is seen that ${}_1\zeta_m/{}_2\zeta_m$ has a minimum value 1.65 when A_f=0.01 m, and as A_f rises, the ratio gradually increase up to 1.81. It indicates that the most vulnerable place to green water is indeed always at the front edge of Box A, regardless of A_f. This phenomenon is quite different from the corresponding one for the 1st-order transient gap resonance revealed by Gao et al. (2020a), and it was found that the most vulnerable place to green water is inside the gap or at the front edge of Box A, which is dependent on the magnitude of A_f.

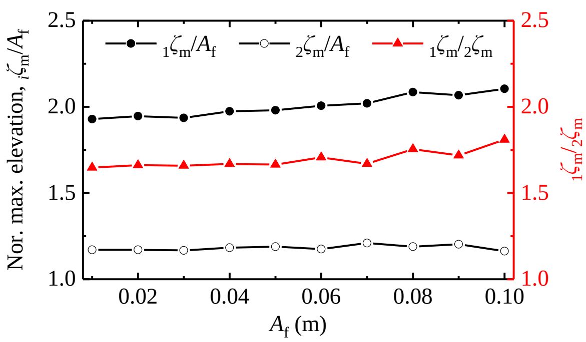

Fig. 8. Comparison of the maximum wave elevations at G_1 and G_2 for various focused wave amplitudes.

4.1.2. High-order harmonics

Based on the analysis technique described in subsection 2.2, the lowest four order harmonic components of the wave elevations for all wave gauges and all incident focused wave amplitudes are extracted. Fig. 9 shows the time series of the lowest four order harmonic components of the wave elevations at G_1–G_3 for A_f=0.03 m, 0.06 m and 0.10 m. Four phenomena are observed from this figure. First, at all the wave gauges, the high-order harmonic components (especially the 2nd-order sum harmonic one) become more and more important as the incident focused wave amplitude increases. Second, due to that the 2nd-order transient gap resonance is triggered by the incident focused wave groups, the high-order fluid motions inside the gap (i.e. at G_2) present the most significant importance compared with those at G_1 and G_3. When A_f=0.10 m, the maximum 2nd-order sum harmonic wave elevation in the gap even exceeds the corresponding 1st-order one (see Fig. 9h). Third, at gauges G_2 and G_3, there exists an obvious difference between the moment of the appearance of the maximum 1st-order sum harmonic wave elevation, $t^{(1)}_m$, and the moment of the appearance of the maximum 2nd-order sum harmonic wave elevation, $t^{(2)}_m$. That is, the appearance of the maximum 2nd-order sum harmonic wave elevation is always obviously later than that of the corresponding 1st -order one at G_2 and G_3. However, for gauge G_1, the maximum 1st- and 2nd-order sum wave elevations appear almost at the same time. Fourth, although the high-order wave elevation becomes more significant with the increase of A_f, all of the 3rd- and the 4th-order sum components and the 2nd-order difference component are still very small compared with the 1st- and the 2nd-order sum components overall. Hence, only the lowest two order sum harmonic components are carefully analyzed in the following.

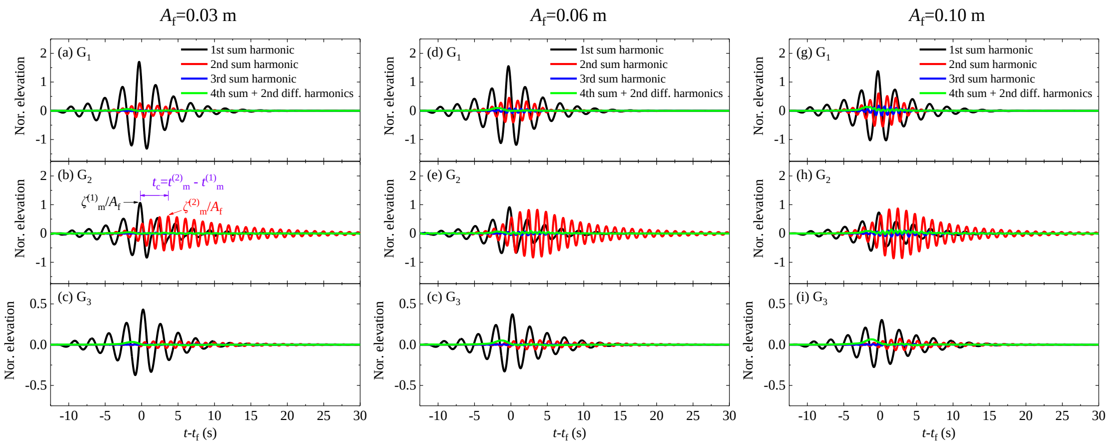

Fig. 9. Time series of the lowest four order harmonic components of the wave elevations at all wave gauges for (a-c) A_f=0.03 m, (d-f) A_f=0.06 m, and (g-i) A_f=0.10 m. All the harmonic components are normalized by A_f. $\zeta^{(1)}_m$ and $\zeta^{(2)}_m$ denote the maximum 1st-order and 2nd-order sum harmonic wave elevations, respectively. $t^{(1)}_m$ and $t^{(2)}_m$ denote the moments of the appearances of

$\zeta^{(1)}{}_{m}$ and $\zeta^{(2)}{}_{m}$, respectively.

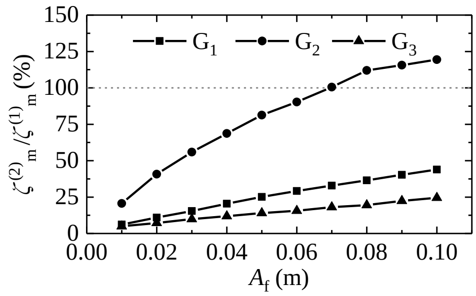

Fig. 10. Ratios of $\zeta^{(2)}{}_{m}$ to $\zeta^{(1)}{}_{m}$ at all wave gauges under various incident focused wave amplitudes.

To quantitatively describe the relative importance of the high-order wave components to the 1st-order one, Fig. 10 presents the ratios of $\zeta^{(2)}{}_{m}$ to $\zeta^{(1)}{}_{m}$ at gauges G_1–G_3 under various incident focused wave amplitudes. The first two phenomena shown in Fig. 9 are quantitatively presented in this figure. Furthermore, it can also be seen that the relative importance of the high-order wave components at G_1 is always higher than that at G_3, although the former is always significantly lower than that at G_2.

4.1.3. Response time and damping time for the first two order sum harmonics

In the actual project, the full understanding about the response time and the damping time of the transient gap resonance is very valuable to guide the berthing/production operation and the evacuation of staff reasonably. Therefore, the response/damping time for the 2nd-order transient gap resonance excited by focused wave groups is studied in this subsection. More specifically, the response/damping time for both the 1st- and the 2nd-order sum harmonic wave elevations in the gap (i.e., at G_2) is investigated. The response time for each harmonic component refers to the time length between the moment that the free surface of each component just starts to move from the rest and the moment that it reaches the corresponding maximum. The damping time is defined as the time length between the moment with the maximum wave elevation and the moment that the wave crest decays to 0.05 times the maximum wave elevation.

Fig. 11 illustrates the time series of the 1st- and 2nd-order sum harmonic wave elevations at gauge G_2 during their response stages. Note that both the 1st- and 2nd-order wave elevations are normalized by their respective maximum values for all the focused wave amplitudes considered, and that the time axis utilized is t-$t^{(i)}_{\mathrm{m}}$ (i=1 or 2). For the 1st-order wave elevations (see Fig. 11a), it can be seen that the response time for all the incident wave amplitudes is extremely close to each other and is around 11.0 s. A similar phenomenon is also observed for the 2nd-order wave elevations (see Fig. 11b). However, the response time for the latter is obviously shorter than that for the former, and is only about 9.0 s. These phenomena are similar to the response time for the total wave elevation inside the gap during the 1st-order transient gap resonance (Gao et al., 2020a), but are quite different from the 1st-order steady-state gap resonance whose response time heavily relies on the amplitude of incident regular waves (Gao et al., 2019b).

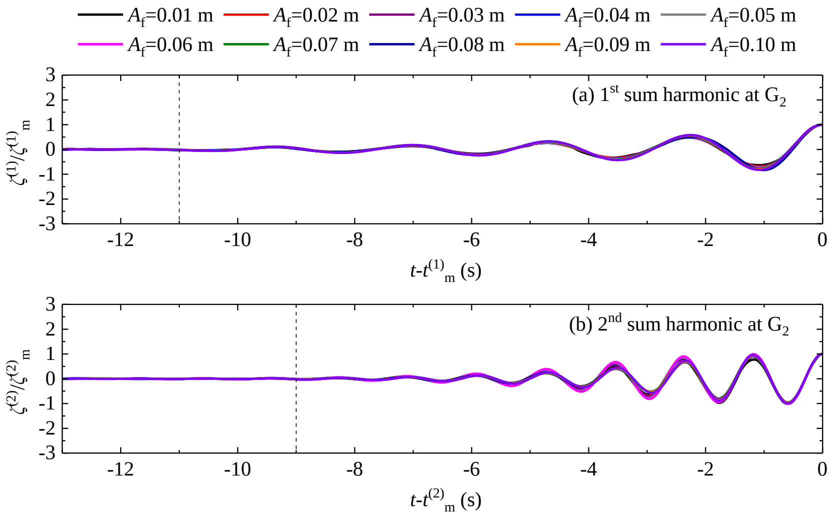

Fig. 11. Time series of the normalized (a) 1st-order and (2) 2nd-order sum harmonic wave elevations at gauge G_2 during their response stages. $\zeta^{(1)}$ and $\zeta^{(2)}$ denote the 1st-order and 2nd-order sum harmonic wave elevations, respectively.

For both the 1st-order steady-state and the 1st-order transient gap resonance phenomena, the total wave elevations in the gap have been revealed to decay in an exponential function during their attenuation stages (Gao et al., 2020a; Gao et al., 2019b). However, aiming at the 2nd-order transient gap resonance phenomenon, whether the exponential-form decay is still valid for the lowest two order sum harmonic wave elevations in the gap is unknown. Through observing Fig. 9b, e and h, the envelopes for both lowest two order sum harmonic wave elevations during their attenuation stages seem to follow the exponential form as well. To examine the above speculation, the lowest two order wave elevations within the gap during their attenuation stages are assumed as

$$\zeta^{(i)}/\zeta^{(i)}{}_{\mathrm{m}} = \bar{a}^{(i)}\cos\left[\omega^{(i)}\left(t-t^{(i)}{}_{\mathrm{m}}\right)+\bar{\varphi}^{(i)}\right]\exp\left[-\delta^{(i)}\left(t-t^{(i)}{}_{\mathrm{m}}\right)\right]\ (i=1\ \text{or}\ 2)\ , \tag{11}$$

in which $\bar{a}^{(i)}$, $\omega^{(i)}$, $\bar{\varphi}^{(i)}$ and $\delta^{(i)}$ are four fitting parameters, and the superscript "(i)" marks out that the variable corresponds to the i^{th}-order sum harmonic wave elevation. If wave elevations decayed in a perfect exponential way from their maximums, $\bar{a}^{(i)}$ and $\bar{\varphi}^{(i)}$ would equate to 1.0 and 0, respectively. Moreover, based on the physical understandings for the lowest two order sum harmonic wave elevations, it can be inferred that the oscillations for them should be dominated by the spectral peak frequency (ω_{P}=2.643 rad/s) and the fluid resonant frequency (ω_{R}=2ω_{p}=5.285 rad/s), respectively.

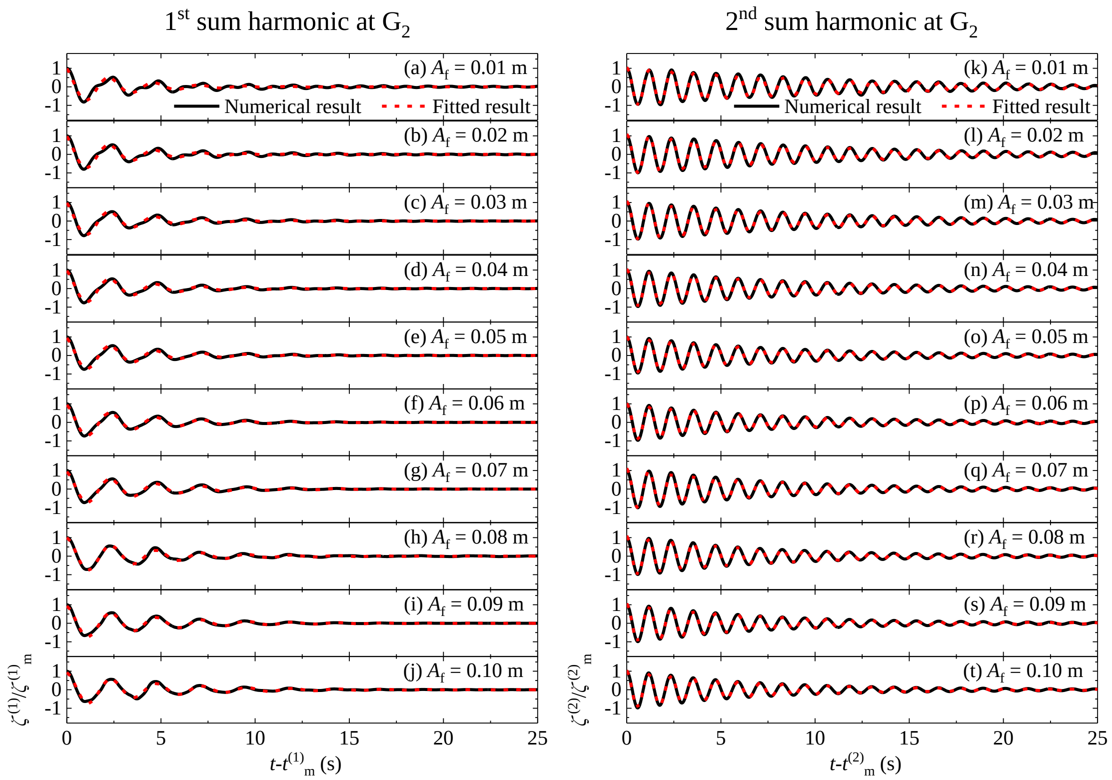

Fig. 12. Comparisons of the lowest two order wave elevations inside the gap extracted by the four-phase combination analysis technique and their corresponding fitted ones by Eq. (11) for the attenuation stage. (a-j) and (k-t) correspond to the 1st-order and the 2nd-order sum harmonic wave elevations, respectively.

Fig. 12 demonstrates the lowest two order sum harmonic wave elevations inside the gap extracted by the four-phase combination analysis technique and their corresponding fitted ones by Eq. (11) for the attenuation stage. It can be visually observed that, for both the lowest two order wave elevations, the fitted wave elevations are consistent well with the extracted ones by the analysis technique, regardless of whether the incident focused wave amplitude is small or large.

Table 1. The fitted values of the parameters in Eq. (11) and the correlation coefficient, R, between the extracted and the fitted curves of the 1st-order sum harmonic wave elevations during the attenuation stage. $Err1$ denotes the error between $\omega^{(1)}$ and the spectral peak frequency, ω_p.

A_f (m)	Fitted values					
	$\bar{a}^{(1)}$	$\omega^{(1)}$ (rad/s)	$\bar{\varphi}^{(1)}$ (rad)	$\delta^{(1)}$	R	$Err1$ (%)
0.01	1.052	2.627	0.348	0.332	0.920	0.605
0.02	1.043	2.612	0.354	0.320	0.946	1.173
0.03	1.037	2.605	0.331	0.309	0.966	1.438
0.04	1.014	2.599	0.301	0.297	0.969	1.665
0.05	0.984	2.599	0.271	0.279	0.970	1.665
0.06	0.970	2.601	0.232	0.264	0.976	1.589
0.07	0.963	2.601	0.227	0.247	0.979	1.589
0.08	1.006	2.621	0.079	0.239	0.984	0.832
0.09	0.953	2.609	0.140	0.227	0.986	1.286
0.10	0.959	2.612	0.107	0.214	0.982	1.173

Table 2. As in Table 1, but for the 2nd-order sum harmonic wave elevations. $Err2$ denotes the error between $\omega^{(2)}$ and the fluid resonant frequency of the gap, ω_R.

A_f (m)	Fitted values					
	$\bar{a}^{(2)}$	$\omega^{(2)}$ (rad/s)	$\bar{\varphi}^{(2)}$ (rad)	$\delta^{(2)}$	R	$Err2$ (%)
0.01	1.063	5.305	-0.039	0.087	0.995	0.378
0.02	1.071	5.304	-0.049	0.093	0.999	0.360
0.03	1.087	5.306	-0.016	0.099	0.999	0.397
0.04	1.062	5.308	-0.014	0.109	1.000	0.435
0.05	1.029	5.306	-0.014	0.118	1.000	0.397
0.06	1.040	5.305	-0.016	0.125	0.999	0.378
0.07	1.094	5.308	0.033	0.129	0.999	0.435
0.08	1.102	5.314	0.062	0.132	0.999	0.549
0.09	1.070	5.310	0.043	0.135	0.999	0.473
0.10	1.053	5.309	0.082	0.140	0.999	0.454

Tables 1 and 2 further list the fitted values for all the four fitting parameters in Eq. (11) and the correlation coefficient between the extracted and fitted curves, R. $Err1$ and $Err2$ in them refer to the error between $\omega^{(1)}$ and the spectral peak frequency (ω_p) and that between $\omega^{(2)}$ and the fluid resonant frequency (ω_R), respectively. For $\bar{a}^{(i)}$ and $\bar{\varphi}^{(i)}$, their respective values are shown to be very close to 1 and 0 for all incident focused wave groups and for both the lowest two order harmonic wave elevations. The correlation coefficients, R, for the 2nd-order sum harmonic components are all larger than 0.990 and even reach up to 1.000. Although the correlation coefficients for the 1st-order sum harmonic components are slightly lower than those for the 2nd-order ones, their smallest value is also high up to 0.920. These fitted results indicate that both the lowest two order wave components in the gap indeed damps out in the form of an exponential function formulated by Eq. (11) during their attenuation stages. It can also be seen from the two tables that both the errors $Err1$ and $Err2$ are extremely small; the largest values for them are only 1.665% and 0.549%, respectively. It directly proves that the oscillations for the 1st- and the 2nd-order sum harmonic wave components during the attenuation stage are indeed dominated by the spectral peak frequency and the fluid resonant frequency, respectively.

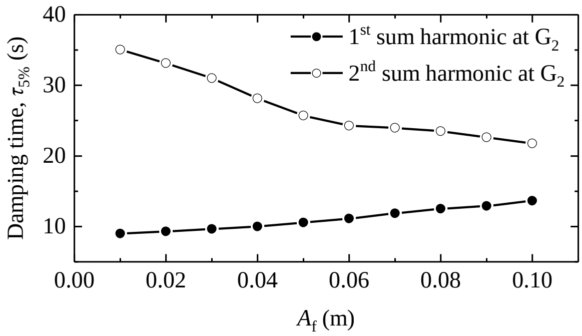

Fig. 13. The damping time for the lowest two order sum harmonic wave elevations at G_2 for various focused wave amplitudes

According to Eq. (11), the time $\tau_{\psi\%}$ that is taken by the lowest two order wave elevations to decline to ψ% of their respective maximums can be easily expressed as

$$\tau_{\psi\%} = -\frac{\ln\left[\psi\% / \left(\bar{a}^{(i)} \cos\bar{\varphi}^{(i)}\right)\right]}{\delta^{(i)}} \quad (i = 1 \text{ or } 2)\,. \tag{12}$$

$\tau_{5\%}$ is chosen here to estimate the damping time. The damping time of the lowest two order wave elevations for all the incident wave amplitudes is presented in Fig. 13. The following two obvious phenomena can be seen. First, the damping time for the 2nd-order wave elevation is always much longer than that for the 1st-order one; the shortest damping time for the former is equal to 21.75 s that appears at the case with A_f=0.10 m, while the longest damping time for the latter is only 13.64 s that occurs at the same case. This phenomenon can be attributed to the fact that the spectral peak frequency of the 2nd-order sum harmonic components is consistent with the fluid resonant frequency of the gap, and hence the 2nd-order sum harmonic components are in the resonance state. Second, the damping time of the lst-order wave elevation is shown to gradually increase with the increase of A_f. On the contrary, for the 2nd-order sum harmonic wave components, their damping time gradually decrease with A_f.

4.2. Horizontal wave forces

4.2.1. Total horizontal wave forces

Fig. 14 presents the comparisons of the time histories of the total horizontal wave forces impacting on the two boxes subjected to the incident crest-focused wave groups with A_f=0.03 m, 0.06 m and 0.10 m. It should be noted here that both the total horizontal wave forces and their harmonic components (they will be shown in the subsection 4.2.2) are normalized by $\rho g h A_f W$ in this article. Two phenomena can be visually observed. First, in the +x axial direction, for all the three crest-focused wave groups, the maximum horizontal wave forces on Box A are shown to be always larger than the corresponding ones on Box B. Contrarily, in the -x axial direction, the former becomes always smaller than the latter. Second, at the attenuation stage, the time histories of the horizontal wave forces acting on both boxes gradually become nearly anti-phase and tend to possess similar amplitudes. It can be explained as follows. The wave groups propagate away from the two boxes in both forms of reflected waves and transmitted waves after the incident focused wave groups hit the two-box system. As shown in Fig. 13, the 1st-order wave elevations inside the gap gradually vanish in around 14 s or shorter time; however, the 2nd-order wave elevations need a much longer time to completely vanish. Hence, the remaining 2nd-order components oscillate inside the gap like a piston, which tends to produce nearly symmetrical flow velocity fields and dynamic pressure fields with respect to the vertical plane located at the middle of the gap.

Obviously, the nearly symmetrical dynamic pressure fields would generate the anti-phase horizontal wave forces with similar magnitudes impacting on the two boxes.

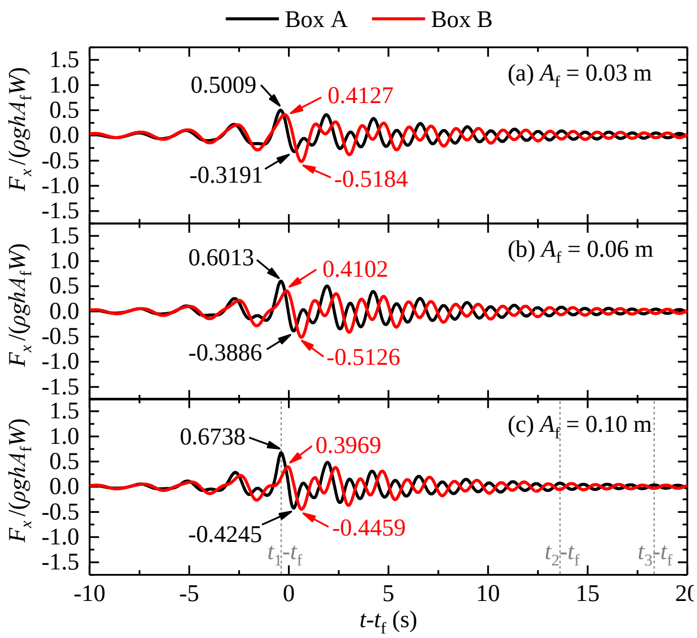

Fig. 14. Comparisons of the time series of the normalized horizontal wave forces on Boxes A and B for the crest-focused wave groups with (a) A_f=0.03 m, (b) A_f=0.06 m, and (c) A_f=0.10 m. t_i (i=1–3) are three moments when both the velocity and dynamic pressure fields around the two-box system will be shown and analyzed, and the specific values for t_i-t_f are listed in Table 3.

Table 3. The specific values of the three moments shown in Fig. 14c, t_i-t_f (i=1–3)

Values of the three moments		
t_1-t_f (s)	t_2-t_f (s)	t_3-t_f (s)
-0.382	13.610	18.338

To show the above explanations more intuitively, both the velocity and dynamic pressure fields in the vicinity of both boxes at the three different moments shown in Fig. 14c and Table 3 are presented in Fig. 15 for the incident crest-focused waves with A_f=0.10 m. It is seen that when the incident focused waves start to hit the two-box system, both the velocity and dynamic pressure fields in the vicinity of both boxes show significant asymmetry with respect to the vertical plane located at the middle of the gap (see Fig. 15a and b). As the incident waves pass far away from the structures, the symmetric tendency with respect to that vertical plane for them becomes more and more obvious (see Fig. 15c–f). Based on the distributions of both the velocity and dynamic pressure fields, it can be inferred that the vertical wave forces on both boxes during the damping stage (including their amplitudes and the phases) tend to become almost identical with each other, and that the wave moments on both boxes during that stage would have almost identical amplitude but become almost anti-phase. These inferences will be proved in subsections 4.3.1 and 4.4.1, respectively.

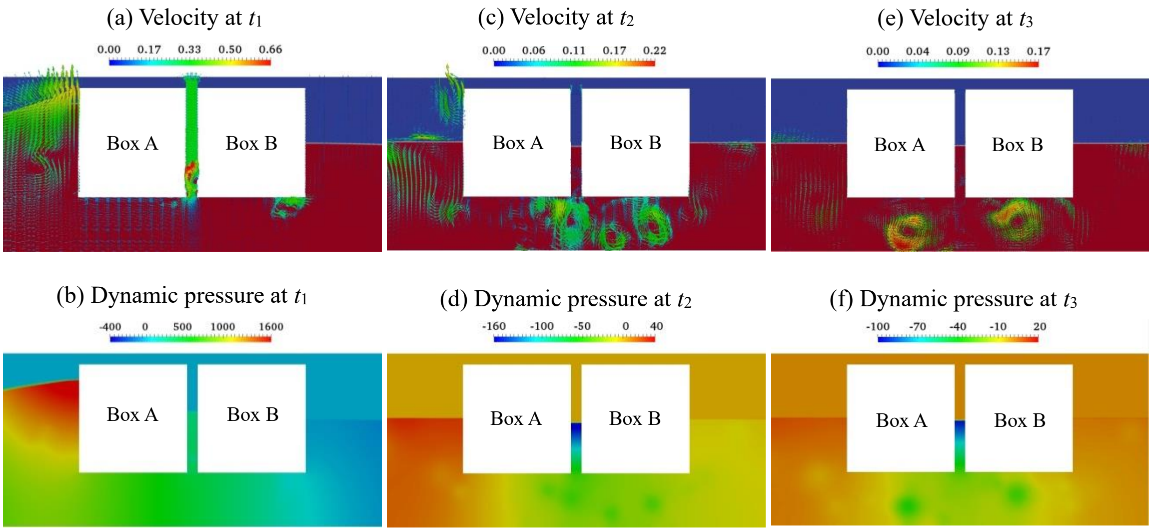

Fig. 15. Velocity and dynamic pressure fields in the vicinity of the two-box system at the three moments shown in Fig. 14c and Table 3. The units of the color bars for the velocity and the dynamic pressure fields are m/s and Pa, respectively.

Fig. 16 further quantitatively compares the normalized maximum horizontal wave forces on Boxes A and B in the same direction. In the +x direction (see Fig. 16a), the normalized maximum horizontal wave forces on Boxes A and B gradually increase and decrease, respectively, with the incident focused wave amplitude. For A_f=0.01 m, the maximum horizontal wave force on Box A is slightly less than that on Box B. When A_f increases to 0.02 m, the two variables become almost identical. As A_f further increases, the maximum horizontal wave force on Box A becomes higher and higher than that on Box B. The ratio of the maximum horizontal wave force in the +x direction on Box B to that on Box A decreases gradually from 113.7% for A_f=0.01 m to 58.9% for A_f=0.10 m. In the -x direction (see Fig. 16b), the normalized maximum horizontal wave force on Box A still increases gradually with A_f, just like the corresponding one in the +x direction. However, the normalized maximum horizontal wave force on Box B does not change monotonically any more. It first increases and then decreases with the increase of A_f, and its maximum value appears at A_f=0.04 m. Furthermore, at the variation range of A_f considered in this article, the normalized maximum horizontal wave force on Box B in the -x direction is always larger than that on Box A. The ratio of the former to the latter first slightly increases and then sharply decreases with A_f, and there is a maximum value of 162.5% at A_f=0.03 m.

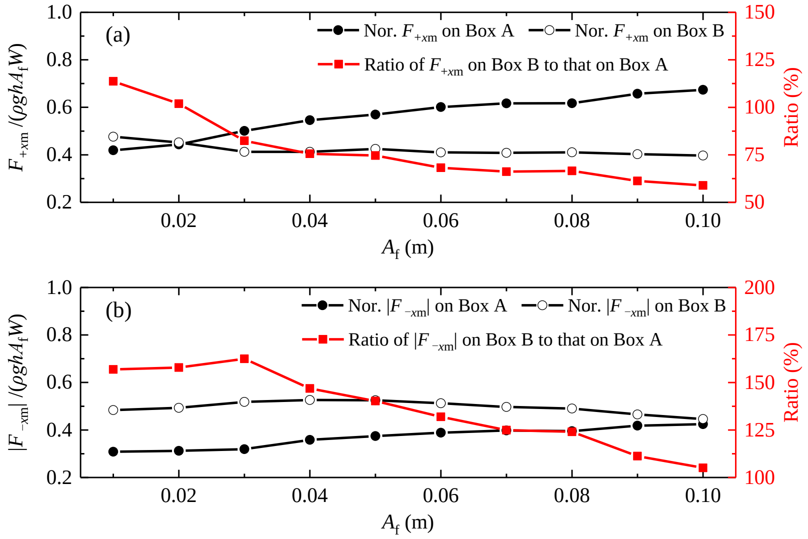

Fig. 16. Comparisons of the normalized maximum horizontal wave forces on Boxes A and B in (a) the +x axial direction and (b) the -x axial direction. F_{+xm} and F_{-xm} denote the maximum total horizontal forces in the +x and the -x axial directions, respectively.

4.2.2. High-order harmonics

Based on the analysis technique shown in subsection 2.2, the lowest four order harmonic components of wave loads on both boxes are also separated. Fig. 17 demonstrates the decomposed lowest four order harmonic components of the horizontal wave forces for the focused waves with A_f=0.03 m, 0.06 m and 0.10 m. It is seen that the magnitudes of the 2nd-order sum harmonic components are significant when compared to those of the 1st-order components even for the incident focused wave group with A_f=0.03 m (Fig. 17a and d). When A_f=0.06 m and 0.10 m (Fig. 17b, c, e and f), the former approaches and even exceed the latter. Similar to the wave elevation inside the gap, for the horizontal wave forces, the magnitudes of both the 3rd/4th-order sum and the 2nd-order difference harmonic components are also extremely small compared with the lowest two order sum harmonic ones. In fact, this phenomenon can also be observed for both the vertical wave force and the wave moment (their lowest four order harmonics are not presented in this article due to limited space). Therefore, only the lowest two order sum harmonic wave loads are analyzed in the following. More specifically, the maximum values of the lowest two order sum harmonic horizontal wave forces in both the +*x* direction and the -*x* direction will be extracted and compared in this subsection.

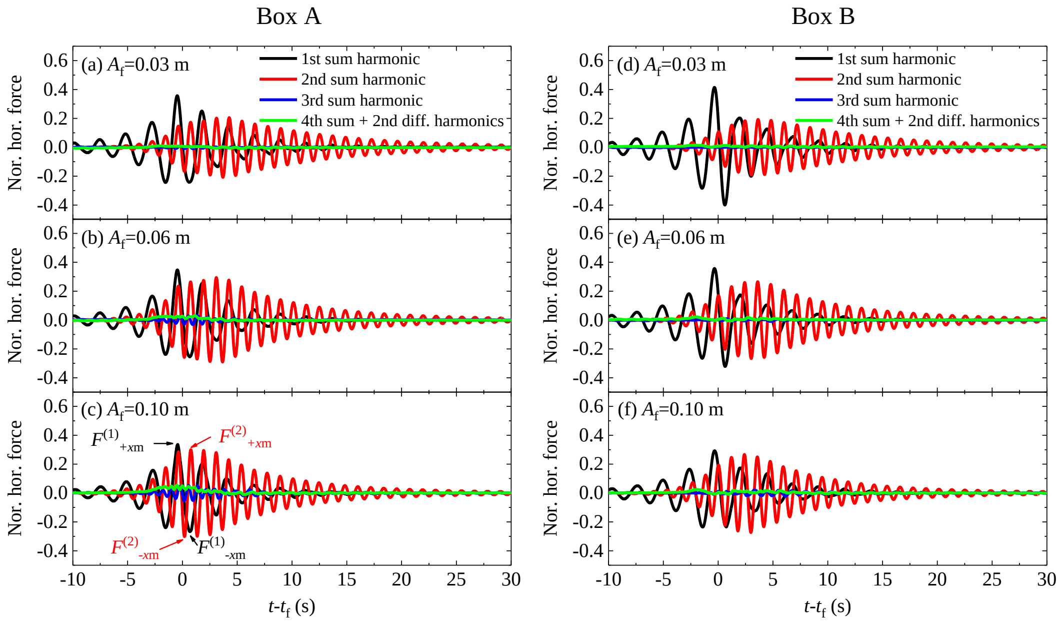

Fig. 17. The lowest four order harmonic components of the normalized horizontal wave forces on (a-c) Box A and (d-f) Box B subjected to the focused waves with A_f=0.03 m, 0.06 m, and 0.10 m. $F^{(i)}_{+xm}$ and $F^{(i)}_{-xm}$ (i=1 and 2) denotes the maximum i^{th}-order horizontal forces in the +*x* direction and the -*x* direction, respectively.

Fig. 18 shows the variations of the normalized maximums of the lowest two order sum harmonic horizontal forces in both the +*x* and the –*x* directions with respect to A_f. The ratios of the 2^{nd}-order to the 1^{st}-order maximum forces in the same direction acting on each box are also presented. For the 1^{st}-order maximum horizontal forces on both boxes (Fig. 18a and b), it is seen that their normalized magnitudes in the +*x* direction are always larger than the corresponding ones in the –*x* direction overall. In addition, for all the 1^{st}-order maximum forces in the +*x* direction on Box A and those in both directions on Box B, their normalized values decrease monotonically with the increase of the incident wave amplitude. However, for the 1^{st}-order maximum horizontal forces in the -x direction on Box A, their normalized magnitudes seem insensitive to the incident wave amplitude. For the 2nd-order maximum horizontal forces on both boxes, their characteristics are completely different from those of the 1st-order ones. For all the incident focused wave amplitudes considered, the 2nd-order maximum horizontal forces in both directions are always almost identical with each other, regardless of Box A or Box B. Furthermore, all of them gradually increase with A_f and eventually approach a specific value in each direction when A_f >0.07 m.

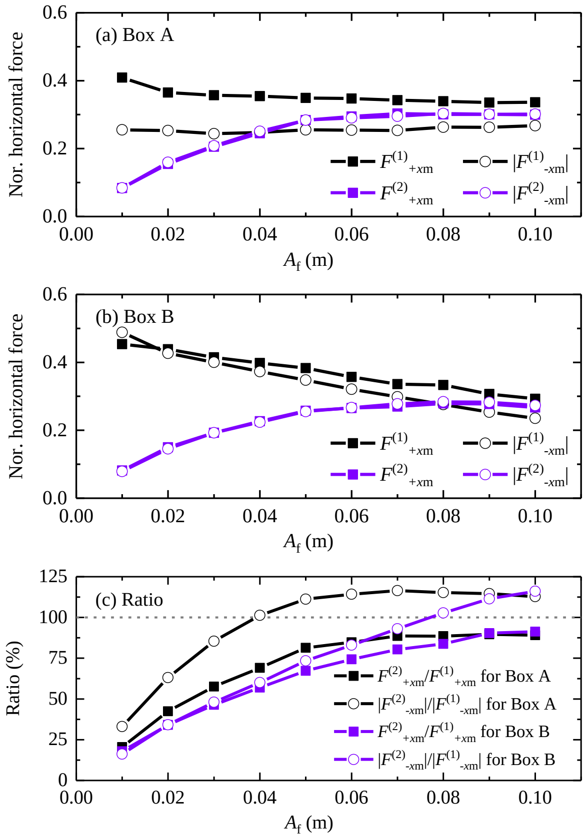

Fig. 18. The normalized maximums of the lowest two order sum harmonic horizontal wave forces in both the +x and the –x directions for (a) Box A and (b) Box B, and (c) the ratios of the 2nd-order to the 1st-order maximum horizontal forces in the same direction for each box

Finally, the relative importance of the 2nd-order harmonic components with respect to the 1st-order ones is quantitatively depicted by the ratios of the 2nd-order to the 1st-order maximum forces in the same direction (Fig. 18 c). It is clearly seen that the importance of the 2nd-order harmonic components becomes more and more significant as A_f increases. In the –x direction, the ratios of the 2nd-order to the 1st-order maximum forces on both boxes can even exceed 110%, while in the $+x$ direction, the ratios are also high up to about 90%. Among the four ratio parameters, $|F^{(2)}_{-xm}|/|F^{(1)}_{-xm}|$ for Box A always has the largest value except at A_f=0.10 m where it is only slightly less than $|F^{(2)}_{-xm}|/|F^{(1)}_{-xm}|$ for Box B.

4.3. Vertical wave forces

4.3.1. Total vertical wave forces

Fig. 19 illustrates the time series of the total vertical wave forces acting on both boxes for A_f=0.03 m, 0.06 m and 0.10 m. Identical to the horizontal forces, both the total vertical wave forces and their harmonic components that will be shown in subsection 4.3.2 are also normalized by $\rho g h A_f W$. Two phenomena can be easily observed. First, the maximum vertical forces on Box A in both the $+z$ and $-z$ directions are always notably larger than the corresponding ones on Box B because of the occlusion effect of Box A on Box B. Second, during the damping stage, the time histories of the vertical wave forces on Boxes A and B tend to become almost overlapped with each other. These two phenomena mentioned above are distinct from the corresponding ones presented in Fig. 14.

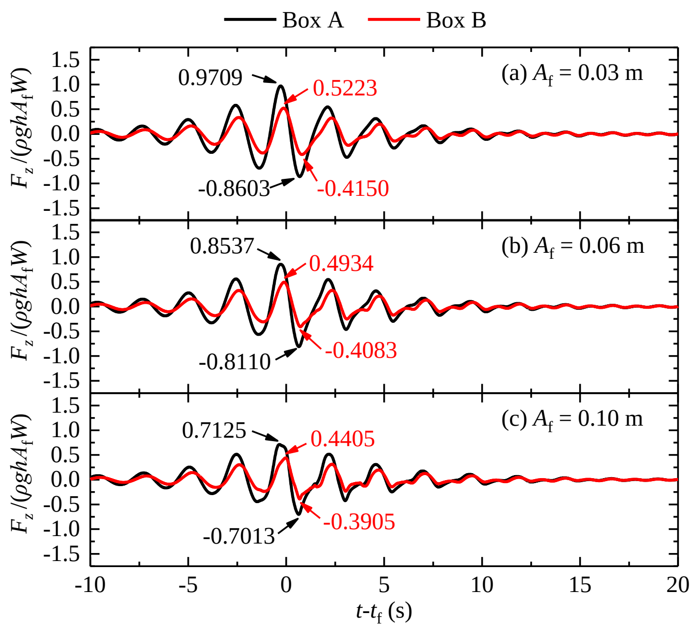

Fig. 19. Time series of the normalized vertical wave forces on Boxes A and B for (a) A_f=0.03 m, (b) A_f=0.06 m, and (c) A_f=0.10 m.

Fig. 20 presents the quantitative comparisons of the normalized maximum vertical wave forces on both boxes in the same direction. In the +*z* direction (Fig. 20a), the normalized maximum vertical wave forces on both boxes decrease monotonically with the incident focused wave amplitude, and the maximum vertical wave force on Box A is always significantly larger than the corresponding one on Box B, although their difference gradually becomes smaller with the increase of A_f. The ratio of the maximum vertical force on Box B to that on Box A gradually increases from 51.7% for A_f=0.01 m to 61.8% for A_f=0.10 m. In the -*z* direction (Fig. 20b), the similar phenomena to those in the +*z* direction are observed, although the specific magnitudes of all the three parameters (i.e., the normalized $|F_{-zm}|$ on Boxes A and B and their ratio) are slightly different from the corresponding ones in the +*z* direction.

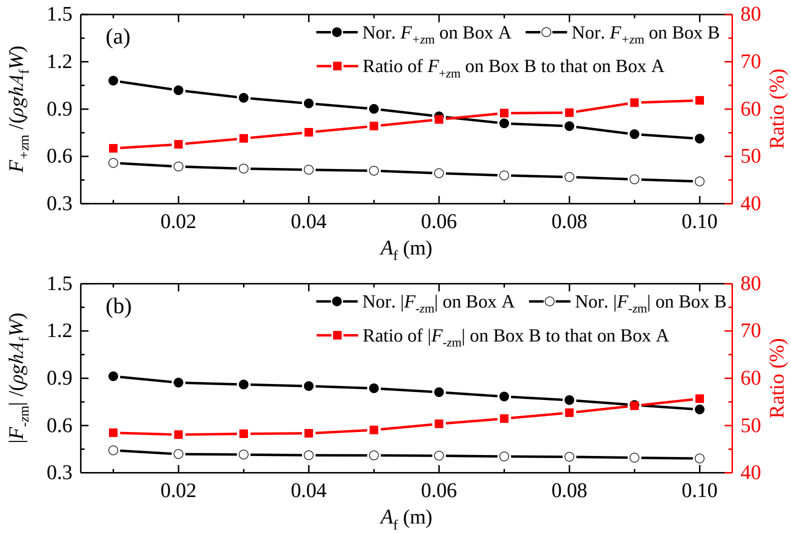

Fig. 20. Comparisons of the normalized maximum vertical wave forces on Boxes A and B in (a) the +*z* axial direction and (b) the -*z* axial direction. F_{+zm} and F_{-zm} denote the maximum total vertical wave forces in the +*z* and the -*z* direction, respectively.

4.3.2. High-order harmonics

Fig. 21 presents the normalized maximums of the lowest two order sum harmonic vertical wave forces in both the +*z* and the –*z* directions for all the incident focused wave amplitudes. For the normalized 1st-order maximum vertical forces on both boxes (see Fig. 21a and b), their magnitudes in the +*z* direction are always larger than the corresponding ones in the –*z* direction. In addition, all of them decrease nearly linearly with A_f. While for the normalized 2nd-order maximum vertical forces on each box, their magnitudes in both directions are almost identical with each other, regardless of whether A_f is large or small. Moreover, all of them increase nearly linearly with the rise of A_f. To quantitatively display the relative importance of the 2nd-order harmonic components, the ratios of the 2nd-order to the 1st-order maximum vertical forces in the same direction for each box are also presented in Fig. 21c. All the four ratio parameters (i.e., $F^{(2)}_{+zm}/ F^{(1)}_{+zm}$ and $|F^{(2)}_{-zm}|/|F^{(1)}_{-zm}|$ for both boxes) are shown to increase nearly linearly with the incident wave amplitude. In addition, among the four parameters, the values of $|F^{(2)}_{-zm}|/|F^{(1)}_{-zm}|$ for Box B are always larger than those of the other three parameters at the whole variation range of A_f. The maximum value of $|F^{(2)}_{-zm}|/|F^{(1)}_{-zm}|$ for Box B is 40.2% which appears at A_f=0.10 m.

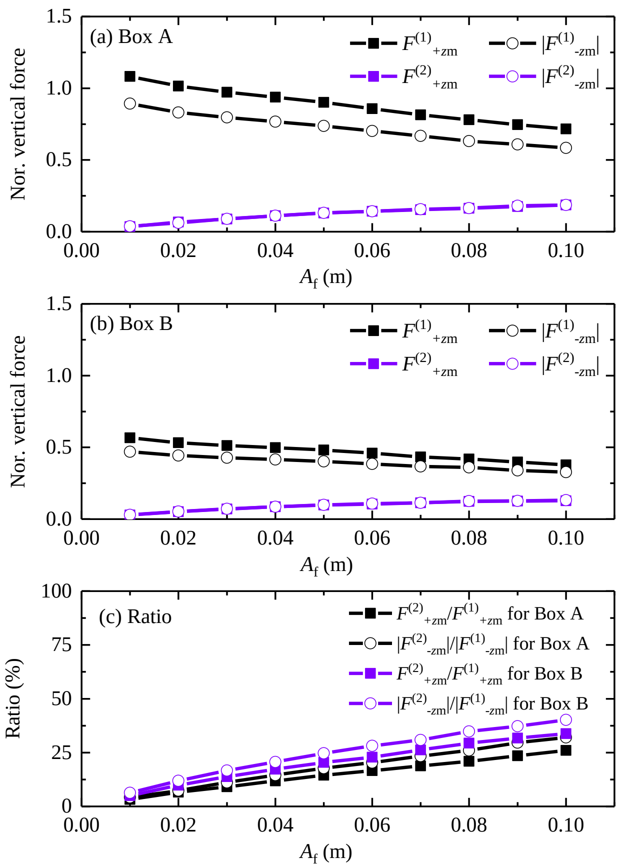

Fig. 21. The normalized maximums of the lowest two order sum harmonic vertical wave forces in both the +z and the –z directions for (a) Box A and (b) Box B, and (c) the ratios of the 2nd-order to the 1st-order maximum vertical forces in the same direction for each box

4.4. Wave moments

4.4.1. Total wave moments

Fig. 22 presents the time series of the total wave moments acting on both boxes for A_f=0.03 m, 0.06 m and 0.10 m. It should be noted here that both the total wave moments and their harmonic components which will be shown in subsection 4.4.2 are normalized by ρghA_fBW. Two phenomena can be easily observed. First, the maximum moments in the $+y$ direction on Box A are always larger than the corresponding ones on Box B for all the three incident wave amplitudes. However, the maximum moments in the $-y$ direction on Box A becomes always smaller than the corresponding ones on Box B. Second, the time series of the vertical wave forces on Boxes A and B during their damping stages tend to have similar amplitudes but become almost anti-phase. Both phenomena are similar to the corresponding ones shown in Fig. 14.

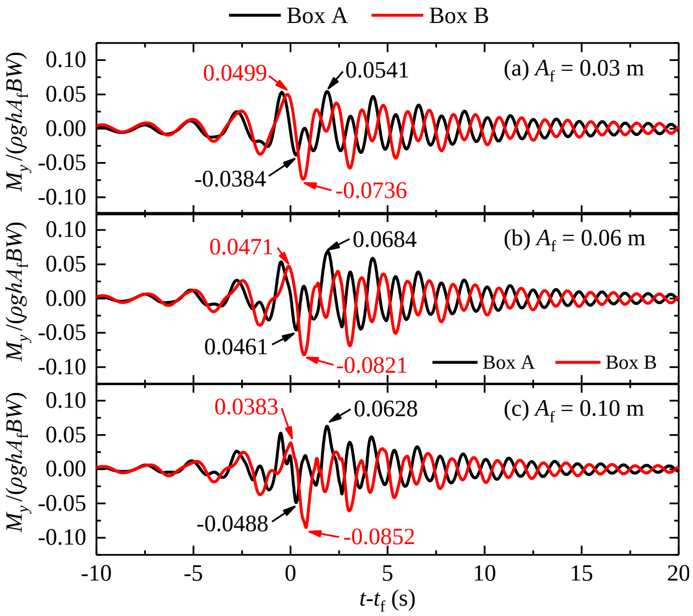

Fig. 22. Time series of the normalized wave moments on Boxes A and B for (a) A_f=0.03 m, (b) A_f=0.06 m, and (c) A_f=0.10 m.

The normalized maximum moments acting on the two boxes in the same direction are further compared in Fig. 23. In the $+y$ direction (Fig. 23a), the normalized maximum moment on Box B is shown to monotonously decrease with the incident wave amplitude. While the normalized maximum moment on Box A first increases and then decreases with the wave amplitude, and its maximum value appears at A_f=0.06 m. Except for the lowest two incident wave amplitudes, the normalized maximum moments in the $+y$ direction on Box B are always smaller than the corresponding ones on Box A, and the ratio of the former to the latter gradually decreases from

116.9% for A_f=0.01 m to 61.0% for A_f=0.10 m. In the -y direction (Fig. 23b), the normalized maximum wave moments on both boxes gradually increase with A_f overall. In addition, for all the incident wave amplitudes considered, the maximum moments in the -y direction on Box B are shown to be significantly larger than the corresponding ones on Box A, and the ratio of the former to the latter fluctuates only slightly around 180%.

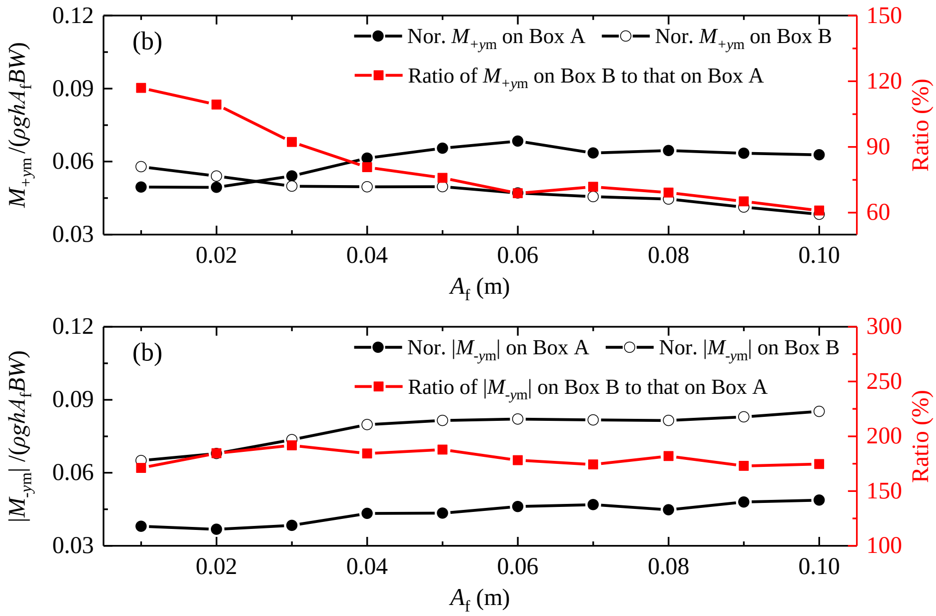

Fig. 23. Comparisons of the normalized maximum wave moments on Boxes A and B in (a) the +y direction and (b) the -y direction. M_{+ym} and M_{-ym} denote the maximum total moments in the +y and the -y direction, respectively.

4.4.2. High-order harmonics

Fig. 24 presents the normalized maximums of the lowest two order sum harmonic wave moments in both the +y and the –y directions for all incident wave amplitudes. The ratios of the 2nd-order to the 1st-order maximum moments in the same direction on each box are also shown. For the 1st-order maximum moments on both boxes (Fig. 24a and b), their magnitudes in the +y direction are basically always larger than the corresponding ones in the –y direction, and all of them monotonically decrease with A_f. However, for the 2nd-order maximum moments on both boxes, their features are distinct from those of the 1st-order ones. The 2nd-order maximum moments in both directions are always extremely close to each other. Moreover, all of them always first rapidly increase and then slightly decline as A_f rises. As for the relative importance of the 2nd-order moment to the 1st-order one, it can be seen from Fig. 24c that the 2nd-order wave moment becomes more and more important as A_f increases. For the four ratio parameters, except $|M^{(2)}_{+ym}|/|M^{(1)}_{+ym}|$ for Box B, all the other three ratio parameters exceed 100% for larger incident wave amplitudes. Even for $|M^{(2)}_{+ym}|/|M^{(1)}_{+ym}|$ for Box B, its maximum value is high up to 94.2% at A_f=0.10 m, very close to 100%. These phenomena indicate that for the 2nd-order transient gap resonance, the 2nd-order sum harmonic wave moment tends to become dominant for larger focused wave groups.

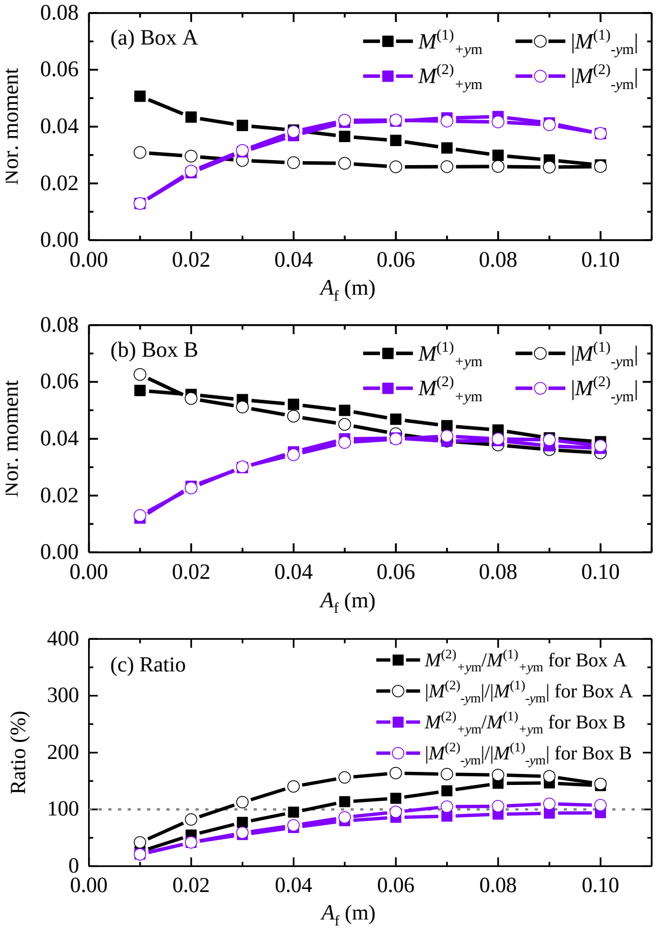

Fig. 24. The normalized maximums of the lowest two order sum harmonic wave moments in both the +*y* and the –*y* directions for (a) Box A and (b) Box B, and (c) the ratios of the 2nd-order to the 1st-order maximum moments in the same direction for each box

4.5. Discussions

In this subsection, the relative importance of the 2nd-order sum harmonic components with respect to the 1st-order ones for all the four physical quantities (i.e., wave elevations, the horizontal wave forces, the vertical wave forces, and the wave moments) is compared in Fig. 25. For the wave elevations, only the curve of $\zeta^{(2)}{}_{m}/\zeta^{(1)}{}_{m}$ at gauge G_2 shown in Fig. 10 is chosen here because of its largest value among the three wave gauges. For each type of wave loads (see Figs. 18c, 21c and 24c), only the curve that corresponds to the overall largest ratios of the 2nd-order to the 1st-order wave loads is selected and reflected in this figure. It can be seen that the importance of the 2nd-order sum harmonic components is the most prominent for the wave moment, and it is the weakest for the vertical wave force. While for the wave elevation and the horizontal wave force, the importance of their 2nd-order components falls in between that for the wave moment and that for the vertical wave force. It should be stressed here that, although the relative importance of the 2nd-order sum harmonic components for the vertical wave force is the weakest among the four physical quantities, the ratio of the 2nd-order to the 1st-order maximum vertical wave forces can reach up to 40.2%, which is still a considerable quantity and cannot be ignored in the calculation of wave loads for the real engineering.

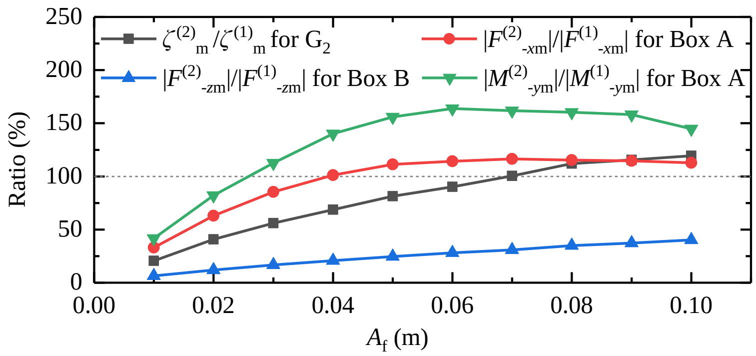

Fig. 25. Comparisons of the ratios of the maximum 2nd-order magnitude to the corresponding maximum 1st-order one for the wave elevation inside the gap, the horizontal wave force, the vertical wave force, and the wave moment.

5. Conclusions

The 2nd-order transient gap resonance phenomenon excited by the incident focused waves is comprehensively investigated here based on the OpenFOAM® model and the "*waves2Foam*" wave-making toolbox. The wave fields both inside the gap and around the two-box system, the three types of wave loads (including the horizontal wave force, the vertical wave force and the wave moment) acting on both boxes, and the relative importance of the 2nd-order wave elevations/loads to the first-order ones are systematically revealed and discussed. In addition, both the response time and the damping time of the lowest two order sum harmonic components of the wave elevations inside the narrow gap are also studied. The research in this article has enriched the knowledges about the transient gap resonance phenomenon.

Main conclusions are drawn in the following:

1. The variation characteristics of the amplification factors of the wave elevations inside the gap, in front of and at the rear of the two-box system with respect to the incident focused wave amplitude are completely different from each other. The amplification factor of the wave elevation inside the gap is insensitive to the incident wave amplitude. However, the amplification factors in front of and at the rear of the two-box system are respectively shown to gradually increase and gradually decrease with the incident wave amplitude. From the perspective of the occurrence of green water on the deck, the location in front of the two-box system, rather than inside the gap, is always the most vulnerable during the 2nd-order transient gap resonance excited by focused wave groups. In addition, the high-order fluid motion inside the narrow gap presents the most significant importance compared with those in front of and at the rear of the two-box system.
2. The response time of the 1st-order wave elevations inside the gap is extremely close to each other and is around 11.0 s for all the focused wave groups considered. Similar phenomenon is also found for the response time of the 2nd-order wave elevations inside the gap, but their response time is only about 9.0 s. During the decaying stage, the oscillations for the 1st- and the 2nd-order sum harmonic wave components are found to be respectively dominated by the spectral peak frequency and the fluid resonant frequency. The damping time of the 1st-order wave elevation and that of the 2nd-order one gradually increases and decreases, respectively, with the incident focused wave amplitude. Moreover, the damping time of the 2nd-order wave elevation is always much longer than that of the 1st-order one.
3. For the three types of wave loads, except the maximum total vertical wave force, both the maximum total horizontal wave force and the maximum total wave moment on Box B are prone to exceed and even become much larger than the corresponding ones on Box A. Although the maximum total vertical wave force on Box B is always lower than the

corresponding one on Box A, the former can still reach up to 61.8% of the latter. These results imply that the maximum wave loads on the downstream structure should be paid the same (and even more) attention with (than) those on the upstream structure during the 2nd-order transient gap resonance. Furthermore, the changing trends of the normalized maximum total wave loads with the incident wave amplitudes depend closely on both the type and the direction of wave loads, and on the structure location (Box A or Box B).

4. Among the four physical quantities studied (i.e., the wave elevation, the horizontal wave force, the vertical wave force, and the wave moment), the importance of the 2nd-order sum harmonic components is the most prominent for the wave moment, and it is the weakest for the vertical wave force. While the importance of the 2nd-order components for the wave elevation and the horizontal wave force falls in between that for the wave moment and that for the vertical wave force. Although the relative importance of the 2nd-order components for the vertical force is the weakest, the ratio of the 2nd-order to the 1st-order maximum vertical wave forces can reach up to 40.2%, which is still a considerable quantity and cannot be ignored in the calculation of wave loads for the real engineering.

Finally, it should be reaffirmed here that the above conclusions are only applicable for the given geometric layout and the given incident focused wave groups considered in this article.

Acknowledgments

This research is financially supported by the National Natural Science Foundation of China (Grant No. 51911530205), the Natural Science Foundation of Jiangsu Province (Grant Nos. BK20201455 and BK20210885), the Natural Science Foundation of the Jiangsu Higher Education Institutions (Grant No. 20KJD170005), the Qing Lan Project of Jiangsu Universities, and the Science and Technology Development Fund, Macau SAR (Grant No. 0050/2020/AMJ). The authors also thank UK EPSRC (Grant No. EP/T026782/1) and the Royal Society (Grant No. IEC\NSFC\181321) for providing partial support for this work.

References

Chen, L.F., Stagonas, D., Santo, H., Buldakov, E.V., Simons, R.R., Taylor, P.H., Zang, J., 2019.

Numerical modelling of interactions of waves and sheared currents with a surface piercing vertical cylinder. Coastal Engineering 145, 65-83.

Chen, L.F., Taylor, P.H., Ning, D.Z., Cong, P.W., Wolgamot, H., Draper, S., Cheng, L., 2021. Extreme runup events around a ship-shaped floating production, storage and offloading vessel in transient wave groups. Journal of Fluid Mechanics 911, A40.

Chua, K.H., Taylor, R.E., Choo, Y.S., 2018. Hydrodynamic interaction of side-by-side floating bodies part I: Development of CFD-based numerical analysis framework and modified potential flow model. Ocean Engineering 166, 404-415.

Ding, Y., Walther, J.H., Shao, Y., 2022. Higher-order gap resonance between two identical fixed barges: A study on the effect of water depth. Physics of Fluids 34, 052113.

Feng, X., Taylor, P.H., Dai, S., Day, A.H., Willden, R.H.J., Adcock, T.A.A., 2020. Experimental investigation of higher harmonic wave loads and moments on a vertical cylinder by a phase-manipulation method. Coastal Engineering 160, 103747.

Fernández, H., Sriram, V., Schimmels, S., Oumeracic, H., 2014. Extreme wave generation using self correcting method - Revisited. Coastal Engineering 93, 15-31.

Fitzgerald, C.J., Taylor, P.H., Taylor, R.E., Grice, J., Zang, J., 2014. Phase manipulation and the harmonic components of ringing forces on a surface-piercing column. Proceedings of the Royal Society London A: Mathematical, Physical & Engineering Sciences 470 (2168), 20130847.

Gao, J., Chen, H., Zang, J., Chen, L., Wang, G., Zhu, Y., 2020a. Numerical investigations of gap resonance excited by focused transient wave groups. Ocean Engineering 212 107628.

Gao, J., He, Z., Huang, X., Liu, Q., Zang, J., Wang, G., 2021. Effects of free heave motion on wave resonance inside a narrow gap between two boxes under wave actions. Ocean Engineering 224, 108753.

Gao, J., He, Z., Zang, J., Chen, Q., Ding, H., Wang, G., 2019a. Topographic effects on wave resonance in the narrow gap between fixed box and vertical wall. Ocean Engineering 180, 97-107.

Gao, J., He, Z., Zang, J., Chen, Q., Ding, H., Wang, G., 2020b. Numerical investigations of wave loads on fixed box in front of vertical wall with a narrow gap under wave actions. Ocean Engineering 206, 107323.

Gao, J., Zang, J., Chen, L., Chen, Q., Ding, H., Liu, Y., 2019b. On hydrodynamic characteristics of gap resonance between two fixed bodies in close proximity. Ocean Engineering 173, 28-44.

Hasselmann, K., Barnett, T.P., Bouws, E., Carlson, H., Cartwright, D.E., Enke, K., Ewing, J.A., Gienapp, H., Hasselmann, D.E., Kruseman, P., Meerburg, A., Müller, P., Olbers, D.J., Richter, K., Sell, W., Walden, H., 1973. Measurements of wind-wave growth and swell decay during the Joint North Sea Wave Project (JONSWAP). Dtsch. Hydrogr. Z A8, 1–95.

He, Z., Gao, J., Chen, H., Zang, J., Liu, Q., Wang, G., 2021a. Harmonic analyses of hydrodynamic characteristics for gap resonance between fixed box and vertical wall. China Ocean Engineering 35 (5), 712-723.

He, Z., Gao, J., Shi, H., Zang, J., Chen, H., Liu, Q., 2022. Investigation on effects of vertical degree of freedom on gap resonance between two side-by-side boxes under wave actions. China Ocean Engineering 36 (3), 403-412.

He, Z., Gao, J., Zang, J., Chen, H., Liu, Q., Wang, G., 2021b. Effects of free heave motion on wave forces on two side-by-side boxes in close proximity under wave actions. China Ocean Engineering 35 (4), 490-503.

Huang, X.H., Xiao, W., Yao, X.L., Gu, J.Y., Jiang, Z.Y., 2020. An experimental investigation of reduction effect of damping devices in the rectangular moonpool. Ocean Engineering 196, 106767.

Iwata, H., Saitoh, T., Miao, G., 2007. Fluid resonance in narrow gaps of very large floating structure composed of rectangular modules, Proceedings of the 4th International Conference on Asian and Pacific Coasts, Nanjing, China, pp. 815-826.

Jacobsen, N.G., Fuhrman, D.R., Fredsøe, J., 2012. A wave generation toolbox for the open-source CFD library: OpenFoam®. International Journal for Numerical Methods in Fluids 70 (9), 1073-1088.

Jiang, S.-C., Bai, W., Tang, G.-Q., 2018. Numerical simulation of wave resonance in the narrow gap between two non-identical boxes. Ocean Engineering 156, 38-60.

Jiang, S.-C., Bai, W., Yan, B., 2021. Higher-order harmonic induced wave resonance for two side-by-side boxes in close proximity. Physics of Fluids 33, 102113.

Kristiansen, T., Faltinsen, O.M., 2008. Application of a vortex tracking method to the piston-like

behaviour in a semi-entrained vertical gap. Applied Ocean Research 30, 1-16.
Kristiansen, T., Faltinsen, O.M., 2012. Gap resonance analyzed by a new domain-decomposition method combining potential and viscous flow DRAFT. Applied Ocean Research 34, 198-208.
Li, X., Xu, L.-y., YANG, J.-m., 2016. Study of fluid resonance between two side-by-side floating barges. Journal of Hydrodynamics, Ser. B 28 (5), 767-777.
Li, Y., Zhang, C., 2016. Analysis of wave resonance in gap between two heaving barges. Ocean Engineering 117, 210-220.
Lu, L., Teng, B., Cheng, L., Sun, L., Chen, X., 2011a. Modelling of multi-bodies in close proximity under water waves—Fluid resonance in narrow gaps. Science China Physics, Mechanics and Astronomy 54 (1), 16-25.
Lu, L., Teng, B., Sun, L., Chen, B., 2011b. Modelling of multi-bodies in close proximity under water waves—Fluid forces on floating bodies. Ocean Engineering 38 (13), 1403-1416.
Miao, G., Ishida, H., Saitoh, T., 2000. Influence of gaps between multiple floating bodies on wave forces. China Ocean Engineering 14 (4), 407-422.
Milne, I.A., Kimmoun, O., Graham, J.M.R., Molin, B., 2022. An experimental and numerical study of the resonant flow between a hull and a wall. Journal of Fluid Mechanics 930, A25.
Molin, B., 2001. On the piston and sloshing modes in moonpools. Journal of Fluid Mechanics 430, 27-50.
Moradi, N., Zhou, T., Cheng, L., 2015. Effect of inlet configuration on wave resonance in the narrow gap of two fixed bodies in close proximity. Ocean Engineering 103, 88-102.
Ning, D., Su, X., Zhao, M., Teng, B., 2015. Hydrodynamic difference of rectangular-box systems with and without narrow gaps. Journal of Engineering Mechanics 141 (8), 04015023.
Ning, D., Zhu, Y., Zhang, C., Zhao, M., 2018. Experimental and numerical study on wave response at the gap between two barges of different draughts. Applied Ocean Research 77, 14-25.
Rodríguez, M., Spinneken, J., 2016. A laboratory study on the loading and motion of a heaving box. Journal of Fluids and Structures 64, 107-126.
Saitoh, T., Miao, G., Ishida, H., 2006. Theoretical analysis on appearance condition of fluid

resonance in a narrow gap between two modules of very large floating structure, Proceedings of the 3rd Asia-Pacific Workshop on Marine Hydrodynamics, Shanghai, China, pp. 170-175.

Song, Z., Lu, L., Li, C., Lou, X., Tang, G., Liu, Y., 2021. An effective resonant wave absorber for long regular water waves. Applied Ocean Research 117, 102966.

Sun, L., Taylor, R.E., Taylor, P.H., 2010. First- and second-order analysis of resonant waves between adjacent barges. Journal of Fluids and Structures 26 (6), 954-978.

Tan, L., Lu, L., Liu, Y., Sabodash, O.A., Teng, B., 2014. Dissipative Effects of Resonant Waves in Confined Space Formed by Floating Box in Front of Vertical Wall, Proceedings of the Eleventh ISOPE Pacific/Asia Offshore Mechanics Symposium, Shanghai, China. Paper No. ISOPE-P-14-080.

Tan, L., Lu, L., Tang, G.-Q., Cheng, L., Chen, X.-B., 2019. A viscous damping model for piston mode resonance. Journal of Fluid Mechanics 871, 510-533.

Taylor, R.E., Sun, L., Taylor, P.H., 2008. Gap resonances in focused wave groups, Proceedings of the 23rd International Workshop on Water Waves and Floating Bodies, Jeju, Korea.

Tromans, P.S., Anaturk, A.R., Hagemeijer, P., 1991. A new model for the kinematics of large ocean waves - application as a design wave, The First International Offshore and Polar Engineering Conference. International Society of Offshore and Polar Engineers (ISOPE), Edinburgh.

Wang, H., Draper, S., Zhao, W., Wolgamot, H., Cheng, L., 2018. Development of a computational fluid dynamics model to simulate three-dimensional gap resonance driven by surface waves. Journal of Offshore Mechanics and Arctic Engineering 140, 061803.

Wang, X.-y., Liu, Y., Lu, L., 2022. Three-dimensional (3D) semi-analytical solution of wave-induced fluid resonance in narrow gaps of caisson-type breakwaters. Ocean Engineering 253, 111305.

Zhang, C., Sun, X., Ding, Z., Chen, L., Ning, D., 2021a. Hydrodynamics of a floating barge adjacent to fixed structure in transient wave fronts. Physics of Fluids 33, 107106.

Zhang, H., Zhou, B., Zang, J., Vogel, C., Fan, T., Chen, C., 2021b. Effects of narrow gap wave resonance on a dual-floater WEC-breakwater hybrid system. Ocean Engineering 225, 108762.

Zhao, W., Taylor, P.H., Wolgamot, H.A., 2021. Design waves and statistics of linear gap resonances in random seas. Flow 1, E11.

Zhao, W., Taylor, P.H., Wolgamot, H.A., Molin, B., Taylor, R.E., 2020. Group dynamics and wave resonances in a narrow gap: modes and reduced group velocity. Journal of Fluid Mechanics 883, A22.

Zhao, W., Wolgamot, H.A., Taylor, P.H., Taylor, R.E., 2017. Gap resonance and higher harmonics driven by focused transient wave groups. Journal of Fluid Mechanics 812, 905-939.

Zhu, R., Miao, G., You, Y., 2005. Influence of gaps between 3-D multiple floating structures on wave forces. Journal of Hydrodynamics , Ser. B 17 (2), 141-147.

Zhu, R., Miao, G., Zhu, H., 2006. The radiation problem of multiple structures with small gaps in between. Journal of Hydrodynamics, Ser. B 18 (5), 520-526.